Catalyst Development for High-Temperature Polymer Electrolyte Membrane Fuel Cell (HT-PEMFC) Applications

Nedjeljko Seselj, Silvia M. Alfaro, Eftychia Bompolaki, Lars N. Cleemann, Tomas Torres,* and Kobra Azizi*

A constant increase in global emission standard is causing fuel cell (FC) technology to gain importance. Over the last two decades, a great deal of research has been focused on developing more active catalysts to boost the performance of high-temperature polymer electrolyte membrane fuel cells (HT-PEMFC), as well as their durability. Due to material degradation at high-temperature conditions, catalyst design becomes challenging. Two main approaches are suggested: (i) alloying platinum (Pt) with low-cost transition metals to reduce Pt usage, and (ii) developing novel catalyst support that anchor metal particles more efficiently while inhibiting corrosion phenomena. In this comprehensive review, the most recent platinum group metal (PGM) and platinum group metal free (PGM-free) catalyst development is detailed, as well as the development of alternative carbon (C) supports for HT-PEMFCs.

1. Introduction

The modern lifestyle entails an ever-increasing, global energy consumption which has significantly sped up the climate change over the course of the past decades. This has become a worldwide concern that has stimulated research on clean, efficient, and more sustainable energy technologies like fuel cells,[1,2] photovoltaics,[3,4] and wind power.[5,6] Fuel cells have been recognized as possible solutions for mobile and stationary applications. The technology combines better fuel utilization than internal combustion engines and minimal CO_2 footprint.[7] Polymer

N. Seselj, S. M. Alfaro, E. Bompolaki, L. N. Cleemann, K. Azizi
Blue World Technologies
Egeskovvej 6C, Kvistgaard 3490, Denmark
E-mail: kaz@blue.world
T. Torres
Department of Organic Chemistry
Institute for Advanced Research in Chemical Sciences (IAdChem)
Universidad Autónoma de Madrid (UAM)
Campus de Cantoblanco, Madrid 28049, Spain
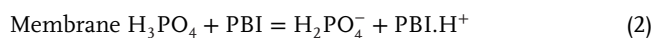E-mail: tomas.torres@uam.es
T. Torres
IMDEA-Nanociencia
c/Faraday, 9, Ciudad Universitaria de Cantoblanco, Madrid 28049, Spain

The ORCID identification number(s) for the author(s) of this article can be found under https://doi.org/10.1002/adma.202302207

electrolyte membrane fuel cells (PEMFC) are already commercially available as (1) auxiliary power units for remote, industrial, and domestic application, and as (2) powertrains from several car manufacturers.[8] This technology is based on perfluorosulfonic acid (PFSA) type membranes (e.g., Nafion) and is often referred to the low-temperature PEMFC (LT-PEMFC) since the operating point is within the range of 60–90 °C. The well-proven membrane material has (1) high conductivity, (2) good chemical stability, (3) mechanical strength and flexibility, and (4) long-term operational durability. The technology is, however, limited to operating at temperatures ≈ 80°C, in order to maintain a highly hydrated membrane. The water molecules within the polymeric backbone of the membrane are crucial for proton conduction, which occurs over the "Grotthuss mechanism".[9,10] Also known as proton jumping, the "Grotthuss mechanism" is the process of proton diffusion through the hydrogen-bonded networks (e.g., water molecules).[11] This technological requirement for water-enabled proton conduction within the polymer electrolyte membrane (PEM) exacerbates system complexities, primarily water and thermal management. Intensive system cooling is required when a LT-PEMFC operates at temperatures of 60–90°C. The fuel and/or oxidant impurity tolerances of the system are quite low in this temperature range, where even minimal contamination, for example, CO, NOx, or sulfur containing species, in either fuel or air, is poisoning the Pt-based catalysts. All these issues, as well as the kinetics for the ongoing electrochemical reactions, are expected to be alleviated at higher temperatures.[12] However, the limitation of proton exchange membrane (PEM) technology, which requires hydration for conductivity, precludes the possibility of operating at higher temperatures. The membrane would get partially hydrated or even fully dry, effectively stopping the ongoing electrochemical reactions. The need of LT-PEMFC for high-purity hydrogen fuel, therefore, presents the issue of hydrogen infrastructure establishment.[13] To successfully commercialize the technology, hydrogen production, distribution, and storage must be realized in a safe, reliable, and affordable manner. Due to these complexities, increasing interest has been put on the high-temperature PEMFC (HT-PEMFC) technology.

To operate a PEMFC at higher temperatures, the main component to be considered is the PEM. The proton conduction has to proceed through a membrane containing a proton-assisting

**ADVANCED
SCIENCE NEWS**

www.advancedsciencenews.com

**ADVANCED
MATERIALS**

www.advmat.de

solvent that has a boiling point higher than the operational temperature of a cell. During operation at temperatures > 100 °C, water flooding and/or dehydration are major problems of LT-PEMFC.[14] It is problematic achieving the balance between the increased water feed to keep the membrane hydrated, and water boiling and evaporating out of the system. Suitable for higher temperature operation ranging from 120 to 180 °C, is the acid–base PEM using a phosphoric acid (PA)-doped polybenzimidazole (PBI) membrane.[15,16] PBI is a class of heat-resistant, heterocyclic thermoplastics that can be doped by several types of acid, such as HCl, HNO_3, $HClO_4$, and H_2SO_4.[17] By PA doping, however, the key features are realized—excellent thermal stability, combined with high proton conductivity and low volatility.[18] Because the phosphorus atom does not have a lone pair of electrons, it cannot form a strong bond with the hydrogen atom, rendering PA as a weak acid (HNO_3 > $HClO_4$ > HCl > H_2SO_4 > H_3PO_4). This results in high proton conductivity/mobility through the PEM, enabling better performance and lower overpotentials toward ongoing electrochemical reactions. Because of a very low PA volatility at HT-PEMFC operating temperature, the PA is retained in the PEM. The H_2SO_4 also possesses low volatility, but being a stronger acid, other MEA components undergo chemical degradation much faster than in the PA system. The PBI/H_3PO_4 is the only membrane to date that meets the US DOE (Department of Energy) criteria for high-temperature membranes. Similarly, as in LT-PEM, the "Grotthus mechanism" is governing the proton conduction within the PA-doped PBI PEM, as shown in the equation below:[19]

$$\text{Anode } H_2PO_4^- + H^+ = H_3PO_4 \tag{1}$$

$$\text{Membrane } H_3PO_4 + PBI = H_2PO_4^- + PBI.H^+ \tag{2}$$

$$\text{Cathode } PBI.H^+ = PBI + H^+ \tag{3}$$

After the fabrication of membrane capable of operating at high temperatures, the next aspect to consider is the membrane electrode assembly (MEA). The MEA consists of two electrodes (anode and cathode) sandwiching the PEM. They are composed of three crucial structures. The thickest electrode layer (200–1000 µm) is the gas diffusion layer (GDL)—highly porous, generally carbon (C)-based structures through which bulk mass transport occurs. A microporous layer (MPL) is the thinnest electrode layer (10–30 µm), containing a denser C structure whose main purpose is to retain the catalytic ink at the electrode surface during fabrication, and therefore, prevent catalyst seeping into the bulk of the GDL. The electrochemically-active catalyst layer (CL) is where the "triple-phase boundary" (TPB) conditions are realized and energy conversion takes place. Depending on the catalyst metal loading, the layer thickness can vary from tens to hundreds of µm. The CL is composed of a C-supported Pt-based nanoparticle (NP) catalyst and is, except in a few cases, immobilized by a suitable polymer binder that attaches the CL to the GDL.[20] The nature of the binder effectively determines the ratio of free to bonded PA molecules, essential for progression of the electrochemical reactions. The amount of PA in the CL has to be balanced in-between the two extremes of drowning the catalyst with too much and disrupting the reaction by having too little PA. These effects are connected with excessive degradation

of Pt and with impeded mass transfer. Furthermore, the presence of free PA at elevated temperatures has a negative impact on the NP catalyst in the electrodes.[21,22] This is reflected by the fact that a Pt catalyst is used almost exclusively on both the anode and cathode, at relatively high loadings of Pt ranging from 0.5 to 1.0 mg cm^{-2}. The CL represents a complex system due to its function requiring efficient mass, energy, and heat transport. In order to attain high activity toward the electrode reaction, the CL has to exhibit a high occurrence of the "triple-phase boundary" points, that is, places where the gaseous reactant meets the proton-conductor (PA within the PBI matrix) and the electron-conductor (C-supported metallic NP) at a Pt surface (**Figure 1**A). The occurrence of the "triple-phase boundary" is highly dependent on the homogeneity of Pt and the binder distribution in the CL. This is directly connected to CL conductivity, thus affecting local current density distribution, and the permeability of the CL.[23] The GDL, MPL, and CL compose a gas diffusion electrode (GDE).

Like in LT-PEMFC technology, catalysts used in HT-PEMFC are Pt-based (often alloyed) NPs, immobilized on various C supports. Catalyst inks are generally formulated with polymeric binders and coated on GDL substrates. There are many methods and compositions for the preparation of MEA depending on the catalyst deposition. There are two common methods used for catalyst ink deposition. The first method involves coating the ink directly onto the membrane (CCM), while the second method involves coating the ink onto the GDL using a catalyst-coated substrate (CCS).[24,25] There are several techniques for catalyst deposition such as spraying (manually or by ultrasonic machine), rolling, sputtering, screen printing, casting, etc.[26] The spraying method is typically used because it provides a good deposition distribution on the surface. Pan et al. suggested impregnating the electrode with 10 wt.% of phosphoric acid for a better electrochemical reaction.[27]

The catalysts used in HT-PEMFC are usually able to tolerate up to 5% (i.e., 50 000 ppm) CO compared to the tolerance level of ≈ 10–100 ppm CO for LT-PEM fuel cells, primarily due to the operational temperature increase enabled by the membrane chemistry.[28,29] Arguably, this is one of the most relevant and beneficial features of the technology. The robustness in fuel selection enables the system to be powered by hydrogen-rich reformate gases, without the need for complex and energy-intensive CO-cleanup. Since the first reports in 1995,[30] HT-PEMFCs have been developed with operating features including little need for humidification, high CO tolerance, and simpler integration with fuel reforming units.

One of the shortcomings of HT-PEMFCs is the sluggish kinetics of oxygen reduction, resulting in decreased power density. Operating with typically-used methanol reformate fuel (69.2% H_2, 22.3% CO_2, 1.4% CO, 6.9% $H_2O(g)$) under ambient pressure, the state-of-art (SoA) performance of commercial Dapozol® or Celtec MEAs is ≈ 0.67–0.70 V at 0.2 Acm^{-2}, or a peak power density of 0.45–0.50 Wcm^{-2} at ≈ 1.0 Acm^{-2}, at comparatively high Pt loadings of 0.7–1.0 mg cm^{-2}. Even when operating on CO_2-containing fuel, the technology is still more environmentally benign than internal combustion engines. This can be further improved when operating on renewable methanol (liquid or gaseous) from power-to-X sources and, therefore, avoiding H_2 infrastructure issues. The concentrated PA presents a
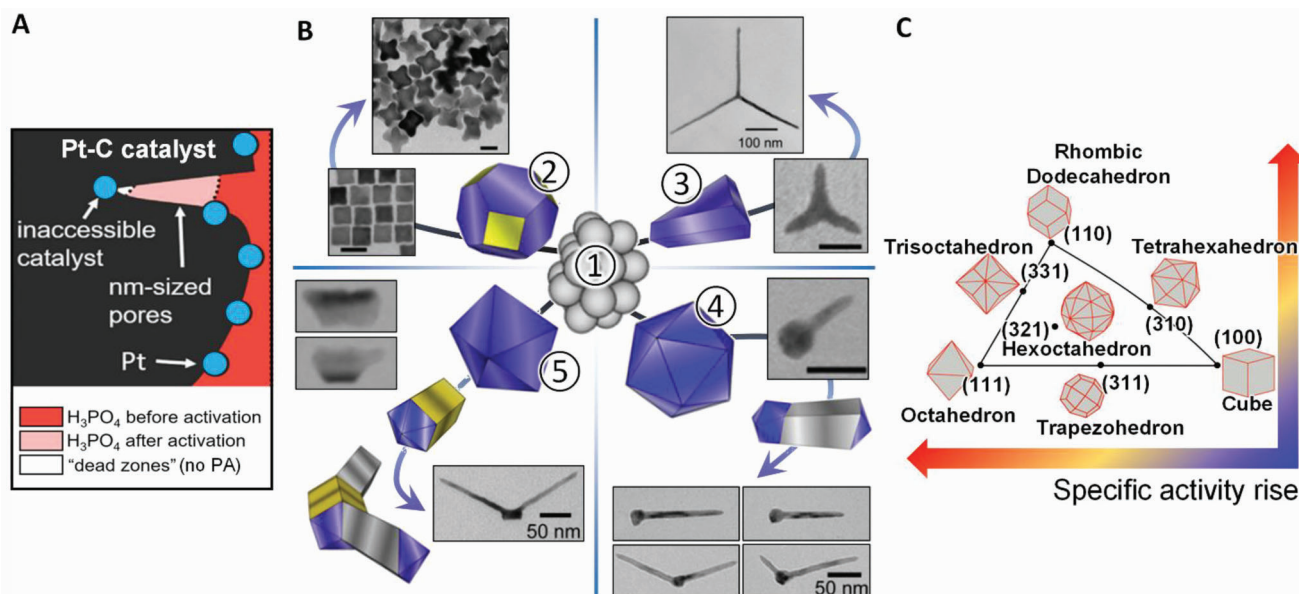
Figure 1. A) Activation of Pt–C catalyst via PA redistribution in the CL. The PA-inaccessible Pt NPs do not create the "triple-phase boundary" and are inactive for the reaction. Reproduced with permission.[60] Copyright 2021, Elsevier. B) Scheme and microscopy images of different Pt NP shape, showing: (1) Pt subcluster nuclei, (2) single crystal cuboctahedron, (3) triangular plate with single twin plane, (4) icosahedron, and (5) decahedron. Reproduced with permission.[61] Copyright 2009, Elsevier. C) Shapes of Pt nano-crystals used as high-activity catalysts for PEMFC. Reproduced under the terms of the Creative Commons CC-BY license.[62] Copyright 201, Frontiers in Chemistry.

catalyst stability issue, especially when operating at elevated temperatures.[31] The relatively high electrode Pt loadings are used to counter various catalyst degradation mechanisms (metal dissolution, catalyst poisoning), which end in the relatively thick catalytic layers (CLs), often measured in the order of 100 µm. This inhibits the mass transport of reactants, and the electronic conductivity of a CL, which eventually can degrade the catalyst. Despite the critical role of CL in HT-PEMFC performance, its electrical conductivity and permeability are not thoroughly described in the literature, unlike the one for LT-PEMFC. Some of the key differences between the two technologies are presented in **Table 1**.

The HT-PEMFC operational durability is accepted as the most critical issue to be addressed before the widespread commercialization of the technology. All the PEMFC components experience a degradation in performance during operation, either reversible or irreversible, leading to a gradual decrease in power output and eventual failure of the system. Chemically, the PEMFC components are subjected to an aggressive environment of strong oxidizing and reducing agents, reaction radicals, electrochemical potentials, and elevated temperatures. The material degradation phenomena include (1) dissolution and (2) sintering of catalyst NPs, (3) C support corrosion, (4) oxidation of polymers, (5) loss of the doping acid, (6) mechanical strain induced by temperature cycling, etc.

The focus of this work is placed on the catalyst aspect of a HT-PEMFC system. The recent development advances have been reviewed and summarized, within the context of (1) material characterization (ex situ/in situ), (2) carbon support (type, graphitization degree, porosity), (3) Pt-based NP catalyst design, including its degradation, (4) platinum group metal (PGM)-free catalyst application and performance in HT-PEMFCs.

2. Catalyst

2.1. Pure Pt Catalysts

Researchers have been studying PEMFC reaction mechanisms for decades to fabricate the most active, and stable catalyst.[47] Platinum (Pt) is still predominantly used as the base metal for various developed materials. Its high activity has been motivating fundamental studies into shape and size-related reaction mechanisms. Various strategies have been developed to improve the performance of Pt-based materials. The development of monometallic Pt catalyst is predominantly focused on the optimization of the (1) NP electrochemically active surface area (ECSA), and (2) C support material. The efficient utilization of ECSA is sought through the NP shape, size, and design control, to engage the most active Pt crystal facets.[48] Since low-temperature (LT) and high-temperature (HT) proton exchange membrane fuel cells (PEMFCs) generally use catalysts with identical elements (platinum-based nanoparticles immobilized on carbon-based support), the fundamental studies of fuel cell reaction kinetics are applicable to both technologies. The HT-PEMFC catalysts face further complexities of PA adsorption at the Pt surfaces, which manifest as (1) reaction kinetics inhibition, (2) non-precious metal dissolution, and (3) enhanced carbon corrosion. Plethora of invaluable fundamental research and material characterization has been done at the LT-PEMFC conditions. Relevant observations are accepted for HT-PEMFCs, although, through the lens of catalyst activity/stability in the PA environment, within the temperature range of 160–180 °C. Duan et al. calculated the reaction energetics (surface adsorption energy, heat of reaction, and activation energy) of ORR on Pt(100) and PtNi(100) surfaces using first-principles density functional

Table 1. Comparison of low-temp. PEMFC versus high temperature PEMFC technologies.

	LT-PEMFC [80 °C]	HT-PEMFC [160 °C]
Membrane	Solid hydrated electrolyte as charge carrier (H⁺).[32]	Acid charge carrier (H⁺), low evap. point → higher temp. can be reached.[14]
	Water required for charge carrier in membrane.[14]	Immobilized acid within membrane matrix, no need for humidification.[33]
	Conductivity depends on optimal humidification and heating & cooling system.[14]	Conductivity depends on acid concentration in the membrane.[14]
Reactions	$H_2 + \frac{1}{2} O_2 \rightarrow H_2O + heat$[34]	
	Sluggish reaction kinetics, ORR particularly.[14]	Higher temp. results in more effective overall reaction kinetic.[14]
	Lower Pt catalyst loading (0.1–0.8 mg cm⁻² for cathode)[35]	Higher Pt loadings due to PA adsorption ($\approx$ 0.8 mg cm⁻²).[36]
Fuels	Pure H_2 fuel (99.999%) & production facilities—too costly.[14] If reformer is used, needs to be coupled with CO filter.[33]	Reforming methanol, natural gas, gasoline, propane (+H_2O). Does not require high-purity H_2.[14]
	Pure H_2 production facilities are still limited.[14]	Simple H_2 reformer (MeOH steam reformer) coupled with stack—efficient heat exchange. Cheaper option.[14]
	Sensitive to fuel impurities.[14,37,38]	Better tolerance of catalyst to CO and fuel impurities, even up to 5%. Tolerance to gas impurities due to higher temp.[14]
	CO sensitive—10 ppm affects performance significantly.[14]	
System	More complex heat exchangers and cooling systems for optimal stack operation.[14]	Simpler heat management due to higher temp. difference stack-environment. Air fan enough for cooling.[14]
	Elaborate water management in stack design.[14] Need for humidification.[33]	Simple water management in stack—only steam from reformer coming out. No need for humidification.[14]
	Energy loss via heat loss. Highly inefficient heat transfers. Heat balance for stack heating, reaction, and cooling.[14]	Heat is used more efficiently due to higher temp. gradient. Heat balance of stack heating, reaction, and reforming.[14]
	Shorter start-up time.[39]	Longer start-up time.[39]
	Lower electrical and cogeneration efficiency (reformate fuel).[33,40,82]	Higher electrical and cogeneration efficiency when fed by reformate[33] Higher system efficiency (than HT PEM + WGS reactor).[33]
Lifetime	Longer lifetime ($\approx$40 000 h).[41]	Shorter lifetime (8000–20 000 h).[14,42]
	Partial membrane drying out/flooding of cell—leads to rapid degradation. Depends on operating conditions, for example, current density, reactant flow rate, gas composition, relative humidity, inlet pressure, and cell temperature.[41,43]	Acid leaching occurs during operation. More pronounced at cycling rather than continuous operation.[14]
	Membrane prone to rapid degradation due to H_2O_2 side-product.[37]	PBI membrane is sensitive to H_2O_2 but (1) its decomposition is inhibited by PA presence and (2) yield of H_2O_2 is lower due to HT and preferred direct 4 e⁻ reaction mechanism ($O_2 \rightarrow H_2O$).[44]
	ECSA loss due to NP loss (aggregation, dissolution, Ostwald ripening, etc.) and/or C support oxidation.[45]	Higher ECSA loss due to HT and highly acidic environment—Pt dissolution/re-deposition at potentials > 0.8 V. Significant oxidation of C support at potentials > 0.9 V.[46]

theory (DFT) methods.[49] Dong et al. conducted a fundamental study in structure-activity relationships and reaction mechanisms of catalytic processes relevant to PEMFC reactions.[50] The ORR study was done on the well-ordered atomic structures, high-index Pt(hkl) single crystal electrodes with superior catalytic activities. Because of the difficulty in obtaining spectra of ORR intermediates during the reaction, especially at high-index facets (HIFs), in situ Raman spectroscopy was employed to investigate ORR processes. Through control and isotope substitution experiments, in situ spectroscopic data of OH and OOH intermediates at Pt(211) and Pt(311) surfaces were successfully obtained. The theoretical simulation and data analysis was conducted on the obtained Raman spectra, and it was deduced that the difference in the adsorption of OOH at HIFs was found to have a significant impact on oxygen reduction reaction (ORR) activity, which deepens our understanding of the reaction mechanism and provides theoretical guidance for designing high-activity ORR catalysts. Furthermore, Hoshi et al. showed the ORR activity is strongly correlated to Pt interatomic distances, in the order of Pt(100) < Pt(111) < Pt(110), when in an acidic environment.[51] Q.

et al studied the detrimental effects of phosphate anion adsorption on low-index Pt single-crystal electrodes, in the presence of varied concentrations of PA. The ORR kinetic current decreased dramatically on Pt(100), Pt(110), Pt(111), even at small addition of PA (1 mM), due to the phosphate anions adsorption onto the Pt active sites. The passivation was found to vary with the specific single crystal surface, following the order of Pt(111) > PtSn(111) > Pt(110) ~ Pt(100). The Pt(110) faceting was found to be the optimal crystal surface for ORR in HT-PEMFC, possessing the smallest charge transfer resistance, while inhibiting the PA poisoning effects the most out of the tested singe crystal electrodes.[52] Correspondingly, the rhombic dodecahedral Pt NPs exhibit the highest, and the cubic shape has the lowest ORR activity in acidic conditions.[53] Cheng et al. studied Pt size-related ORR activity by using a Se film on the C support to seed < 2nm Pt NPs and sub-nano clusters. As-synthesized material exhibited both superior performance and durability.[54]

In terms of surface and morphology, anisotropic structures[55] and a high degree of crystallinity[56] promote stability, whereas high-energy surface nanostructures result in a better distribution

of active sites on accessible HIFs.[57] Various nanostructures involving 1D nanowires, 2D nanoplates, and 3D polyhedrons, and nano-frames have been reported to improve the utilization of atomic Pt, increasing the amount of accessible active sites.[57] The greater intrinsic activity of these structures is assigned to low-coordinated Pt atoms (steps, kinks, edges, and corners).[58] In addition, ultra-thin (≈ 3 nm) Pt nanowires and 3D Pt nano-assemblies allow for the formation of free-standing membranes, enabling a direct transfer of such films to electrodes as CLs (Figure 1B,C).[55,59]

Among Pt nanocrystals, Pt multi-cube nanocrystals, whose surface is mostly enclosed by Pt(100) facets are shown to result in enhanced ORR mass activity.[63] This is due to a combined effect of low resistance, induced by flat surfaces, and more active sites, as a result of HIFs.[63] Highly concave Pt nano-frames with high index facets (749) presented an excellent electrocatalytic performance[56] via an increased surface-to-volume ratio. This was due to the higher amount of atomic steps, kinks, corners, and edges assigned to the concave shape of the Pt nano-frame.[56] Anisotropic Pt multi-pods with plenty of HIFs displayed doubled ORR activity and durability, compared to commercial Pt–C,[64] due to strong NP binding to the C support via multiple anchoring points.[65]

Efforts to enhance the intrinsic activity of pure Pt and reduce the content of precious group metal (PGM) catalysts, while maintaining fuel cell (FC) performance, have been ongoing to achieve large-scale technology commercialization.[66–68] Aiming at high activity, DFT studies show that a pure Pt catalyst with maximized surface sites of generalized coordination number (GCN) between 7.5 and 8.3 could be ideal.[69] The above would tailor Pt particle size in the range within 1.8–3 nm.[69] Specific activity for ORR was found to hit a maximum for NPs with a diameter of 3 nm, confirming theoretical predictions.[70]

Application of Pt nano-designed structures for HT-PEMFC is so far restricted due to limited tunability of the catalyst structure on micro/macro-scale, resulting in non-optimal CL properties.[71] Electrode preparation procedures need to be optimized to enhance Pt ECSA utilization. Interactions with the PA electrolyte should be taken into consideration, as electrode reactions may be hindered by phosphate anion adsorption and challenged by gas transport due to the lower solubility of oxygen in PA.[25,26] Recently, the use of effective binder materials with microporosity and acid interactive functionalities has been shown for HT-PEMFCs,[72] resulting in preferential retention of PA in the CL.[72] This leaves room for improving the tunability of Pt nanostructures for application in HT-PEMFC CLs.

2.2. PGM Binary Alloys

Optimizing the Pt crystal phase, NP size, shape, and catalyst morphology, to enhance its intrinsic activity and stability, has been reaching a threshold in decreasing the material cost. Some novel nanostructures and elaborate synthesis routes ensured high-performing materials, at the cost of being unfeasible for industrial upscale and commercial application. The research, therefore, turned toward nanostructured Pt-alloy electrocatalysts, which often exhibited excellent catalytic activities for the ORR. Today, Pt alloys, core-shell, and Pt-skin structures are dominant
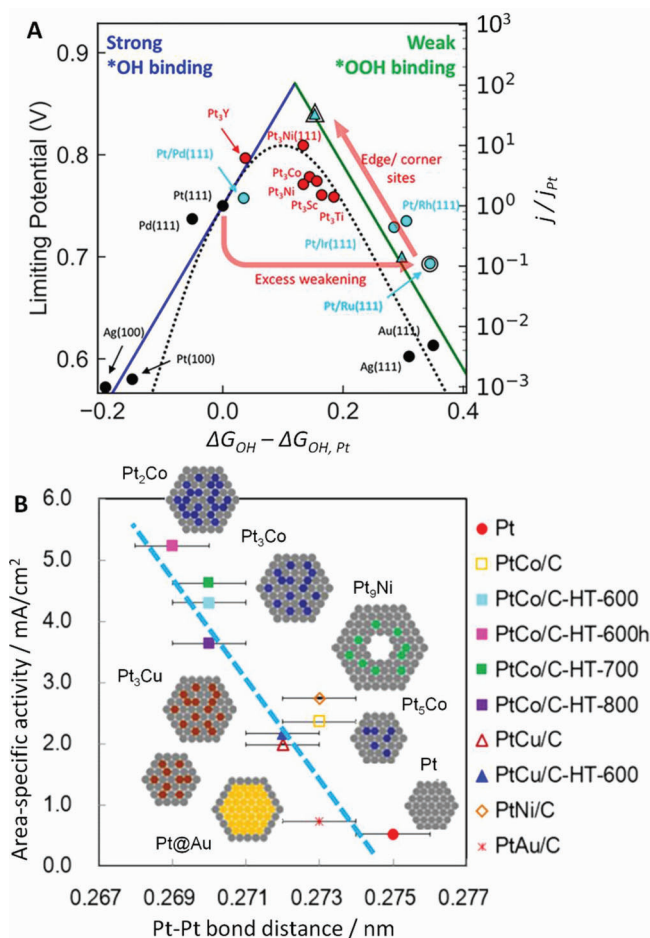
Figure 2. A) Volcano plot representing binding energies of *OH and *OOH species to Pt and Pt alloy surfaces. Reproduced with permission.[87] Copyright 2018, American Chemical Society. B) Monotonic rise of Pt and Pt alloy area-specific activities with decreasing Pt–Pt bond distances. Reproduced with permission.[88] Copyright 2016, American Chemical Society.

choices for ORR.[73] The Pt-based bimetallic and trimetallic electrocatalysts are effective ways of improving ORR activity and stability while reducing the material cost. The alloying elements are often chosen for their own catalytic activities. The performance of these systems has been attributed to the collaborative action between the metals, termed as bifunctional catalysis.[74] Alloying Pt with other metals can improve the NP catalytic activity and enhance its durability, via the so-called "anchor effect".[37] A popular approach is alloying Pt with transition metals such as cobalt (Co), nickel (Ni), iron (Fe), and copper (Cu), to form Pt-rich surface NPs. The alloying element is typically chosen based on a volcano plot, which represents binding energies of *OH and *OOH species to Pt and Pt alloy surfaces (**Figure 2**A). The resultant material is usually formed by either a specific etching process or the dissolution of transition metal atoms during FC operation. This catalyst morphology is often referred to as a core-shell or Pt-skin structure. Several of these catalysts are already commercially used.[75]

Like in LT-PEMFCs, carbon-supported Pt-based NPs are the main catalyst type used in HT-PEMFC. The main difference is

**ADVANCED
SCIENCE NEWS**

www.advancedsciencenews.com

**ADVANCED
MATERIALS**

www.advmat.de

in the increased noble metal loading (≈ 1.0 mg cm^{-2}) of HT-PEMFC, when compared to the typical LT-PEMFC Pt loadings (0.1–0.4 mg cm^{-2}).[36] This is due to the partial electrolyte flooding of the catalyst layer and anion adsorption which then impedes the ORR in concentrated PA. To reduce the noble-metal loading of a FC, Pt alloyed catalysts like PtCo and PtNi can be used. The stability of these materials is questionable under FC operating conditions. Transition metals are known to form oxides and hydroxides that dissolve from the electrode surface.[36] Carbon-supported Pt-transition metal alloy catalysts are, however, often used in HT-PEMFCs. This is mainly due to the enhanced catalytic activity,[76] credited to Pt structural changes caused by alloying, which often result in shortening the Pt–Pt interatomic distances.[77] The alloy layer underneath the Pt-skin can shift the d-band vacancy of Pt upward or downward, depending on the secondary metal of choice.[36] This affects the specie-specific adsorption energies on Pt atoms, making it a feasible way of fine-tuning the reaction mechanism activities in PEMFCs. The research in the field was carried out since the 1970s within the phosphoric acid fuel cell (PAFC) development, now transferred to PBI-based HT-PEMFCs.[78,79] The studies focus on performance enhancement mechanisms in HT-PEMFCs—whether the alloying improved the ORR activities, or if the phosphates adsorption was inhibited on the NP surfaces.[15]

The two important issues concerning Pt alloys in HT-PEMFCs are (1) particle stability, and (2) modified adsorption energies at reactive surfaces. First, all Pt alloys with non-noble metals will de-alloy to a certain degree under HT-PEMFC conditions.[15] Pt alloys with transition or refractory metals such as chromium (Cr) and zirconium (Zr) were originally believed to be stable enough for these harsh conditions, resulting in extensive research into this group of alloys for application in PAFCs. Although some of these alloys have demonstrated extraordinary chemical stability against corrosion (especially when alloyed with refractory metals such as Cr and Zr), they are still electrochemically unstable, as verified by the leaching out from alloys in PAFCs.[80] Pt-alloy catalysts with different alloy cores, therefore, eventually get similar Pt-skin surfaces after a period of FC operation, irrespective of the alloy type. The underneath alloy cores can, however, still affect Pt overlayer properties via the ligand and/or strain effect, altering the ORR performance.[81]

Second, the alloying metal in Pt–M can change the molecular adsorption properties of a series of species on transition metal-based surfaces via the same anchoring atom.[82] This "scaling relationship" likely applies to the O$_2$ and phosphate ion adsorption on Pt via adsorbed oxygen (O^{ad}). The tuning of binding strengths is, therefore, possible in one direction—either stronger or weaker. The target for these systems is weaker binding energies, for both phosphates and the O$_2$ adsorption, to achieve better ORR activity, and therefore, lower Pt loadings. As reported, the optimal binding energy for the *OOH species is ≈ 0.2 eV weaker than that on Pt(111).[83] This substantiates the possibility of finding a Pt-alloy catalyst that has high ORR activity at less phosphate poisoning. PtCo, PtNi, PtFe, and Pt-gold (Au) have been reported to show enhanced ORR performances and weaker phosphate adsorptions, ideal for operation in HT-PEMFC.[84–86]

Although the doped PBI membrane contains most of PA, it is also added to the CL to facilitate proton transfer. This unfortunately increases the adsorption of PA on Pt, poisoning the active

sites and degrading its activity.[89] The Pt surface energy modifications and geometric configurations are some of the mitigation strategies to combat phosphate anion adsorption. Pt alloys with Ni and Co demonstrated a down-shift in the d-band center, compared with pure Pt. This results in weaker PA adsorption. PtAu alloys, on the other hand, exhibit an up-shifted d-band center of Pt. The better ORR activity of PtAu than pure Pt was explained by the geometric effect, where PA anions adsorb at "three-fold sites" on the Pt surface.[52] Their presence is much lower in the PtAu alloy surface due to Pt atoms being isolated by Au atoms.[90]

The "third-body effect" is proposed as a strategy to suppress Pt surface anion adsorption.[91] This entails pre-adsorbing molecules on the Pt surface, which decreases the availability of "three-fold sites", effectively suppressing phosphoric anion adsorption. Since pre-adsorbates themselves partially cover Pt active sites, the catalytic activity, therefore, depends on the extent of pre-adsorbate coverage. Li et al. studied the optimum pre-adsorbate coverage by correlating the Pt ORR activity with pre-adsorbate coverage of the surface. The ORR activity of Pt decreases monotonically with increasing pre-adsorbate coverage. The maximum activity in PA occurs at pre-adsorbate coverages of $\approx 20\%$.[89]

The modification of specie-specific adsorption energies plays an important role in the context of CO-poisoning inhibition as well. Since hydrogen oxidation occurs at the Pt sites, water dissociation happens at the oxophilic metal sites. The adsorbed CO intermediates at the Pt sites can be oxidized by the oxygen-containing species at the neighboring oxophilic metal sites. Ruthenium (Ru) is often selected as the oxophilic metal in binary or multi-metallic (ternary & quaternary) catalysts.[92] Since Ru is even rarer than Pt, PtRu alloy is not commercially feasible for a large-scale application. Consequently, an alternative approach based on the Ru substitution by Co to form PtCo alloy catalysts has been proposed to resolve the CO-poisoning inhibition problem.[93]

2.2.1. Pt–Co

The alloying element Co changes the position of the d-band center of Pt by modifying the electronic structure of neighboring Pt atoms, and affecting the Pt–CO bond strength, promoting the cleavage of C–H bond at lower potential. Furthermore, the presence of Co oxides at the catalyst surface provides an oxygen atom source, necessary for the oxidation of adsorbed CO at Pt surfaces. A large number of studies on PtCo alloy NPs, having different morphologies, for example, spheres, wires, or ribbons, have been produced by conventional wet-chemistry methods.[94] Research on different PtCo NP structures is still ongoing.[95–97]

Motivated by reducing the high Pt loading in HT-PEMFC, Shroti et al. reported a facile preparation of a PtCo alloy NPs supported on multi-wall (MW) carbon nanotubes (CNTs).[79] The activity of this catalyst toward the ORR, and its tolerance to PA poisoning was compared to other electrocatalysts (similar support, NP size, and spatial distribution), where one was based on Pt and the other a physical mixture of Pt and Co. The superior PtCo alloy was applied at the cathode, where performance and stability showed the potential to decrease the Pt loading of HT-PEMFC electrodes without compromising performance.

**ADVANCED
SCIENCE NEWS**

www.advancedsciencenews.com

**ADVANCED
MATERIALS**

www.advmat.de

Durst et al. performed a defined series of acid and heat treatments on benchmark PtCo catalysts, succeeding in fabricating three different nanostructures of interest for ORR electrocatalysis.[98] The Pt-skin nanostructures were made of (1) a single pure Pt layer, covering the Pt–Co structure, and (2) 2−3 Pt atomic layers atop the alloy core. It was shown that the Pt-skin reverted toward the Pt-skeleton upon contact with an acid electrolyte. This caused a large decrease in the Co content (> 30%) but with no release of the lattice strain of the core material, signifying an unaltered Pt d-band shift. They also pointed out that the alternation of heat and acid treatments (conditions found in HT-PEMFC) can strongly decrease the core Co content and potentially contaminate the MEA.

Wang et al. reported a neural-like network of PtCo NPs connected by CNTs, able to show outstanding performance in PEM-FCs. More impressively, the material showed negligible degradation in an electrochemical half-cell (ORR), and PEMFC operation as a cathode catalyst.[99]

Zhao et al. successfully "confined" PtCo NPs in mesoporous carbon structures derived from the zeolitic imidazolate framework. The mesoporous structure prevented both (1) detachment and (2) agglomeration of NPs, while the catalytic activity toward ORR was not compromised.[100]

Rao et al. prepared carbon-supported PtCo alloy NPs of various Pt:Co atomic ratios (1:1, 2:1, 3:1, and 4:1), which were then evaluated as cathode catalysts in HT-PEMFCs. Improved performance was observed for Pt:Co atomic ratios of 1:1 and 2:1.[78]

Garrick et al. studied the ORR-specific activity of PtCo catalyst, observing a continued voltage increase with cycling despite a noticeable loss in Co content (up to 70%). This was explained by changes in the adsorbed oxygen species and their coverage as the transition metal leached out and the Pt skin grew thicker.[40]

Huang et al. reported a synthesis of Pt alloy integrated in a Co−N-nanocarbon matrix by a multiscale design principle, to achieve more efficient ORR. This Pt-integrated catalyst showed 11.7 times higher mass activity (1.52 A mg_{Pt}^{-1} at 0.9 V vs RHE), than the commercial Pt catalyst, retaining 98.7% of stability after 30 000 potential cycles, and delivering power density of 0.98 W cm^{-2} at 0.6 V as cathodic catalyst in a FC, outperforming the commercial Pt−C (Johnson Matthey (JM) 40 wt%) (0. 78 W cm^{-2}) catalyst.[73]

Carbon-supported Pt and Pt alloys with different structures, compositions, and morphologies were studied by Kaito et al. Regardless of the catalyst atomic ordering or morphology (core−shell or random alloy), the ORR activity was primarily reliant on the Pt−Pt bond distances. The PtCo, having the shortest Pt−Pt distance, exhibited the highest ORR activity, with ≈ 10- and 6-times higher surface and mass activities, respectively, compared to a commercial carbon-supported Pt electrocatalyst. They found a monotonic increase in catalytic activity toward ORR with decreasing Pt−Pt distance, the scheme in Figure 2B.[88]

PtCo alloys, similarly to PtNi catalysts, have demonstrated great ORR activities. They are the only advanced ORR catalysts successfully used in mass-produced FC vehicles (FCVs), like Toyota Mirai.[101] Compared with other Pt–M (M = transition metal) materials and the widely used Pt–C NPs, PtCo alloy catalysts provide a better balance between activity and durability.[75] Papadias et al. investigated the durability of PtCo PEMFC cathodes with different initial Co contents. The study revealed that even with

significant (27%–50%) Co loss, the specific activity of PtCo catalysts toward ORR remained higher than 1000 μA cm^{-2} at 0.9 V versus RHE, exceeding 650 μA cm^{-2} of pure Pt NPs.[102]

Lei et al. demonstrated the synthesis of PtCo, PtNi, and PtFe NPs through the simple solution-phase route, finding that PtCo was the most active for the ORR between them.[103] A similar observation was made by Wang et al.[104]

2.2.2. Pt–Ni

He et. al. studied the effect of phosphate anion poisoning of cathodic Pt-based catalysts in PAFC by observing the kinetics of the ORR in the presence of varied concentrations of PA.[105] A PtNi alloy catalyst was used to reduce phosphate poisoning. The study showed the poisoning effect was much less severe on PtNi than on pure Pt catalyst.

Mamlouk et al. tested PtCo, PtNi, and PtFe alloys for ORR, with a composition of 1:1 in atomic ratios.[106] They claimed only the PtNi catalyst exhibited better activity compared to the conventional Pt catalyst. However, no long-term FC tests were done to argue the stability of the produced alloys in HT-PEMFC.
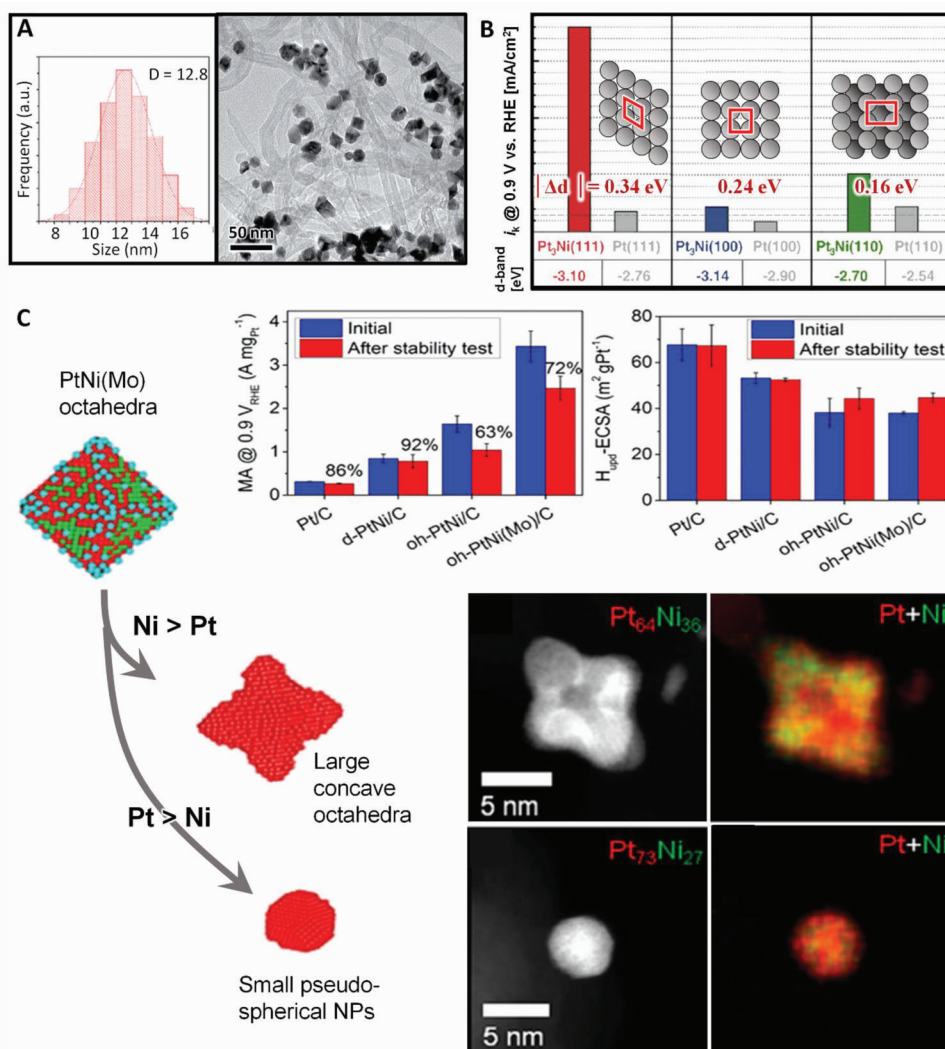
Becknell et al. studied the Pt-skin structure stability in PtNi nano-frames by estimating the ECSA via CO and H_2 underpotential deposition region adsorptions ($ECSA_{CO}$, $ECSA_{HAD}$).[107] The high PtNi ORR activity catalyst had a preferred Pt-skin surface and high $ECSA_{CO}/ECSA_{HAD}$ ratio, while PtNi nano-frames with low activity had a low $ECSA_{CO}/ECSA_{HAD}$ ratio, closing into the pure Pt catalyst. The study presents a convenient tool for predicting PtNi stability and ORR activity.

Gong et al. successfully synthesized PtNi dumbbell-shaped particles, which did not show increased ECSA, compared to commercial C–Pt, but were able to achieve higher ORR activity.[108] The enhanced electrocatalytic performance is attributed to:

1) PtNi dumbbell-shaped particles forming multiple 2D nanosheet structures, providing a relatively large area of HIFs, which possess highly active sites.
2) Incorporation of a transition metal into Pt nanostructures can adjust the surface electronic properties of Pt, which can accelerate the reduction of O_2 molecules. The lattice strain in the PtNi alloy leads to the downshift of the Pt d-band center, which weakens the adsorption energy between Pt and O^{ad}, therefore, improving the ORR performance. Since the presence of Ni decreases the chemical adsorption of oxygen-containing species, the CO poisoning tolerance is also improved by the alloying effect.

Stamenkovic et al. carried out a fundamental study on PtNi alloys with excellent performances toward ORR.[109] The PtNi(111) surface had a 90-fold higher activity toward ORR than Pt monometallic catalyst (**Figure 3**B), due to the (1) favorable downshift of the d-band center, and (2) the arrangement of Pt-rich surface atoms with the second Ni-rich atomic layer. The weak interaction between the Pt surface atoms and non-reactive oxygenated species increased the number of active sites for O_2 adsorption.

Chen et al. used the rotating disk electrode (RDE) technique to test PtNi nano-frame catalysts which exhibited a 36-fold enhancement in mass activity (5.7 A mg_{Pt}^{-1} at 0.9 V vs RHE) and

**ADVANCED
SCIENCE NEWS**

www.advancedsciencenews.com

**ADVANCED
MATERIALS**

www.advmat.de

Figure 3. A) TEM images of octahedral PtNi-CNT catalyst, with corresponding NP histogram. Reproduced with permission.[115] Copyright 2018, Royal Society of Chemistry. B) Specific activities of the PtNi and pure Pt surfaces for ORR. Reproduced with permission.[109] Copyright 2007, The American Association for the Advancement of Science. C) Pt ECSA and mass activities before/after stability test for Pt/C, PtNi-C, and PtNi(Mo)-C catalysts. Scanning TEM (STEM) images and EDX composition maps of alloy catalysts, after a stability protocol. Reproduced with permission.[116] Copyright 2019, American Chemical Society.

22-fold increase in specific activity, compared to 5 nm Pt catalyst by Tanaka (TKK).[110]

Li et. al. synthesized ultrafine jagged Pt nanowires prepared through leaching out Ni from Pt–NiO core-shell nanowires, having the highest mass activity (13.6 A mg_{Pt}^{-1} at 0.9 V vs RHE) in the RDE measurement recorded to date.[111] The reactive molecular dynamics simulations suggested that highly stressed, undercoordinated, rhombus-rich surface configuration of the jagged nanowires was responsible for unprecedented ORR activity. These shape-controlled catalysts are, however, still in development due to the difficulties in their scale-up.

Han et. al. demonstrated high ORR performance and durability of a family of dealloyed PtNi NP catalysts.[112] They found that smaller size, less-oxidative acid treatment, and annealing significantly reduced Ni leaching, while encouraging Pt-surface homog-

enization, all resulting in improved stability and higher catalytic ORR activity.

Some of the recent research focuses on the development of octahedral PtNi NP alloys (Figure 3A,C).[48] Wang et. al. synthesized a composite catalyst consisting of the self-made PtNi octahedral NPs on the carbon support.[113] The material was used as both an anode and cathode catalyst in a MEA, with a 6% mass addition of IrO_2 and RuO_2 (highly active catalysts for water electrolysis) at the anode. With peak power density of 0.95 W cm^{-2} at 0.679 V, it outperformed a commercial Pt catalyst (JM) in LT-PEMFC. More importantly, PtNi octahedral NPs showed significantly increased durability under continuous cell reversal conditions, which occurs when a current load is applied to the FC under fuel starvation conditions. Anodic polarization occurs, where its potential increases and surpasses cathodic potential, resulting in the cell reversal condition. The typical FC ongoing HOR and ORR are

**ADVANCED
SCIENCE NEWS**

www.advancedsciencenews.com

**ADVANCED
MATERIALS**

www.advmat.de

then replaced by water electrolysis and carbon oxidation reactions at the cathode and anode, respectively. Cell reversal, therefore, causes severe carbon corrosion, usually resulting in irreversible cell degradation and loss in FC performance.[114]

2.2.3. Pt–Fe

Choi et al. synthesized PtFe NPs in a block copolymer matrix, achieving a carbon shell formation around the NPs.[117] This catalyst had extremely high Pt mass activity of 0.9 A mg_{Pt}^{-1}, at an ultra-low Pt loading of 0.01 mg cm^{-2}.

Yang et al. reported a silica-assisted pyrolysis method for the reduction of PtFe NPs.[118] The silica is removed after the pyrolysis, PtFe NPs are etched, resulting in a hollow structure. Alternative synthesis routes for PtFe NPs are the impregnation-reduction method and single precursor pyrolysis.[119,120] Higher processing temperatures lead to the formation of ordered structures, more favorable for ORR.

Chung et al. studied depositing a thin Pt-based shell (one or several atomic layers) upon the Fe metal core, as core-shell structures to improve Pt utilization and to achieve remarkable activity and stability.[121] They demonstrated that the ORR of such core-shell NPs was largely affected by their sub-surface, rather than the bulk composition. The study showed that the electrocatalytic properties of Pt NPs can be enhanced by Fe-doping surface modification.

Xiao et al. designed a hybrid PtFe electrocatalyst consisting of atomically dispersed Pt and Fe single atoms and PtFe alloy NPs.[122] The power density generated was 1.08 W cm^{-2} at 2.0 A cm^{-2}, 3.7 times higher than the commercial C−Pt when applied as cathodic catalysts in LT-PEMFC. More importantly, the material showed excellent durability, with 97% activity retention after 100 000 cycles.

Hu et al. reported a simple strategy to combine structurally ordered intermetallic PtFe NPs with N-doped carbon confinement.[123] The NPs were formed in situ, which benefited in homogeneous particle distribution on carbon support, and prevented the NPs from agglomeration or detachment. The material exhibited excellent performance, as well as enhanced anti-poisoning capability toward CO, SO_x, and PO_x when assembled as cathode catalysts for HT-PEMFCs, a peak power density of 384 mW cm^{-2} at 0.6 V is reached at 160 °C. The demonstrated strategy provided a novel insight into the fabrication of stable, active, and economical HT-PEMFC catalysts.

2.2.4. Pt–Cr

Yano et al. synthesized monodispersed Pt and PtM (M = vanadium (V), Cr, Fe, Co, and Ni) alloy carbon-supported NPs by the one-pot synthesis.[124] The average NP diameters ranged from 2.0 to 2.5 nm, regardless of the catalyst-loading level (from 10 to 55 wt % on carbon black (CB)). The area-specific ORR activities on PtM were found to be 1.3 to 1.8 times higher than on pristine Pt catalyst (0.82 mA cm^{-2} at 0.8 V vs RHE). The ORR activity increased in the order Pt < PtNi < PtFe < PtCo < PtV < PtCr.

Antolini et al. have reviewed the stability of Pt-alloy catalysts used in LT-PEMFCs and noted that PtCr and PtCo tend to exhibit greater stability than PtV, PtNi, and PtFe NPs. That puts Cr as a promising alloying candidate, considering PtNi catalyst is already being successfully used in HT-PEMFCs.[101]

Sakthivel et al. prepared a carbon-supported PtCr bimetallic catalyst by a simple co-reduction route in formaldehyde.[125] The catalyst had an average NP size of ≈ 4.6 nm but exhibiting two fold higher specific and mass activities for ORR than Pt, under half-cell conditions. More importantly, PtCr showed higher resistance toward metal leaching in sulfuric acid than PtNi. The average PtCr NP size grew from 4.5 to 8 nm after 7000 degradation cycles, compared to Pt NPs which increased from 4.5 to 30 nm. This indicated a significant enhancement in catalyst durability.

2.2.5. Pt–Pd

Besides abundant transition-metals, Pt is also alloyed with more precious metals when performance or extended durability is paramount. Palladium (Pd) is alloyed with Pt in a variety of nanostructures.[126–128] Yusof et al. studied binder varying ratios (1–7) in a carbon-supported 20–40 wt% PtPd cathodic HT-PEMFC catalyst.[129] The results showed that the ORR performance was influenced by the (1) distribution of metals at the carbon surface, (2) carbon particle size, and (3) interaction between binder and catalysts. The 30 wt% PtPd catalysts exhibited the best performance and the highest durability at 170°C, yielding a power density of 1.30 W cm^{-2} at only 20 μg_{Pt} cm^{-2} loading. This impressive performance with an ultra-low metal loading highlighted a promising catalyst for HT-PEMFC application.

Al-Tememy et al. examined the performance of MWCNT-doped graphene (G) nanoplatelet-supported PtPd bimetallic catalyst in the HT-PEMFC.[126] The performance of the catalyst was tested in the H_2/air and reformate/air FC. The MWCNT-G-PtPd catalyst outperformed the commercial C−Pt, with 390 and 310 mW cm^{-2} at 160°C, and 0.6 V for H_2/air and reformat/air FC, respectively.

Sasaki et al. reviewed the performance of Pt monolayer on palladium (Pd) NPs for the ORR and described the mechanisms of their high activity and stability through core-shell NP structure design.[130] They recently demonstrated that the ORR activity and stability of the catalysts could be further improved with some novel nanostructured cores via optimization of their surface orientation, composition, and morphology.

Brouzgou et al. studied carbon-supported PtM (M = Ir, Pd) electrocatalysts, with different atomic ratios (Pt:M = 3:1, 1:1, 1:3), toward CO tolerance and durability.[131] It is found that Pd shows higher CO tolerance than Pt, while $PtPd_3$ exhibits the highest CO tolerance ability, even after being exposed to 400 ppm of CO for 9 h. Although Pt_3Ir showed higher CO tolerance than Pt, it failed during prolonged testing (>6 h). Finally, it is found that PtIr and PtPd exhibit excellent durability even after 5000 cycles of accelerated stress test, while Pt_3Pd and PtPd presented the highest mass activities (340 and 410 mA mg_{Pt}^{-1} respectively at 0.9 V), 4 and 5 times higher than the commercial pristine Pt catalyst (82.75 mA mg_{Pt}^{-1}).

2.2.6. Pt–Ir

Wesselmark et al. used well-defined thin-film model electrodes, to study the stability of Pt and Pt on Ir as FC cathode catalysts.[132] All samples with Ir showed an increased stability over samples with sole Pt during cyclic corrosion test between 0.6 and 1.2 V versus the reversible hydrogen electrode (RHE). For thin layers of Ir, the initial activity for the ORR was equal or superior to that of pristine Pt, however, for thicker Ir films it was somewhat lower. HAD and CO stripping were used to estimate the ECSA, indicating that Ir can indeed stabilize Pt in the cathodic CL.

Bekmezci et al. synthesized carbon-supported PtIr NPs.[133] The hydrogen oxidation reaction (HOR) peak current density was calculated to be 61.98 mA cm^{-2}. The PtIr catalyst also had higher ECSA and CO poisoning tolerance, than C–Pt. The FC testing showed the PtIr NPs provided improved methanol oxidation, compared to C–Pt.

Ahn et al. studied the carbon corrosion reaction under cell reversal conditions, motivated by the goal of increasing the FC durability.[114] They investigated the effect of IrO_2 as a catalyst additive to commercial C–Pt catalysts containing different Pt loadings (20, 40, and 60 wt%). These catalyst configurations were applied for the HOR and tested over 50 cycles of cell reversal conditions. The performance with and without IrO_2 as an additive was assessed, concluding that IrO_2 effectively prevented catalyst degradation caused by the cell reversal. They also observed that catalysts with higher Pt loadings were more resilient to cell reversal conditions.

2.2.7. Pt–Ru

Although PtRu has been established as one of the most feasible CO-tolerant electrocatalyst (**Figure 4**), its stability at high cost hinders commercial application. Dissolution and dealloying are identified as the main degradation mechanisms during potential cycling, with preferential dissolution of Ru. Developing a bifunctional anodic electrocatalyst with both high CO tolerance and stability is challenging due to the vulnerability of non-noble metals to dissolve under the acidic environment of PEMFCs.[134]

Hengge et al. investigated stability, chemical composition, and structure of a PtRu catalyst alloy with a nominal ratio of 1:1.[135] The same catalyst particles were analyzed before and after potential cycling experiments by identical location TEM. Ru proved to be less stable during the electrochemical treatment, however, its presence in the PtRu catalyst alloy accounted for easier removal of CO from the Pt surface, as demonstrated by a lower CO stripping voltage.

Alpaydin et al. studied the effect of MWCNT and G nanoplatelet-based (GNP) catalyst supports on the performance of HT-PEMFC.[137] It was found that PtRu/MWCNT-GNP hybrid material is a suitable catalyst for HT-PEMFC. The hybrid material was synthesized by microwave irradiation method. The group, however, did not test the long-term durability of such a catalyst.

2.2.8. Pt–Au

Au nanostructures have been extensively studied and their application as CO oxidation catalysts is well known. Moreover, pos-
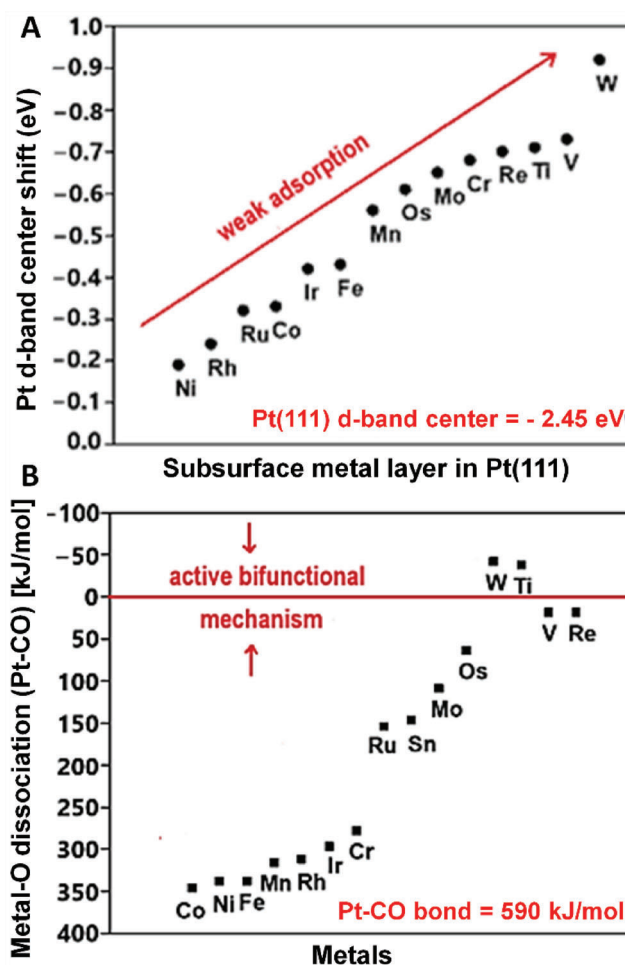

Figure 4. Simulation studies of A) Pt d-band shift with Pt-skin coverage by metal monolayer. B) Difference between metal-O dissociation and Pt–CO energies. Reproduced under the terms of the Creative Commons CC-BY license.[136] copyright 2021, The Authors. Licensee MDPI, Basel, Switzerland.

sessing an atomic diameter close to Pt, Au is an easy candidate for core material in core-Pt shell NP architectures.

Lee et al. studied the phosphate adsorption characteristics and its effect on ORR for various carbon-supported catalysts (Pt, PtCo, $Au_{core}–Pt_{shell}$).[86] The degree of phosphate adsorption for each catalyst was evaluated by: (1) the addition of PA during cyclic voltammetry (CV), (2) monitoring the evolution of phosphate adsorption peaks (0.25–0.3 and 0.5–0.65 V vs RHE), and (3) the decrease in the Pt oxidation current (@ 0.9 V). The phosphate adsorption was found to be the weakest for the $Au_{core}–Pt_{shell}$, compared to other catalysts. The relative ORR activity with PA addition was significantly smaller for Co-containing alloy catalysts (18.2%) and larger for $Au_{core}–Pt_{shell}$ (30.2%) compared with the commercial Pt catalyst (27.8%).

Seselj et al. synthesized Au_{core}/Pt_{shell} graphene-immobilized catalyst (G-Au@Pt) through chemical and surface chemical reactions (**Figure 5**A–E).[138] The 9 nm Au@Pt core@shell NPs with atomically thin Pt shells were covalently immobilized on G via L-cysteine amino-acid, serving as a NP anchoring linker.
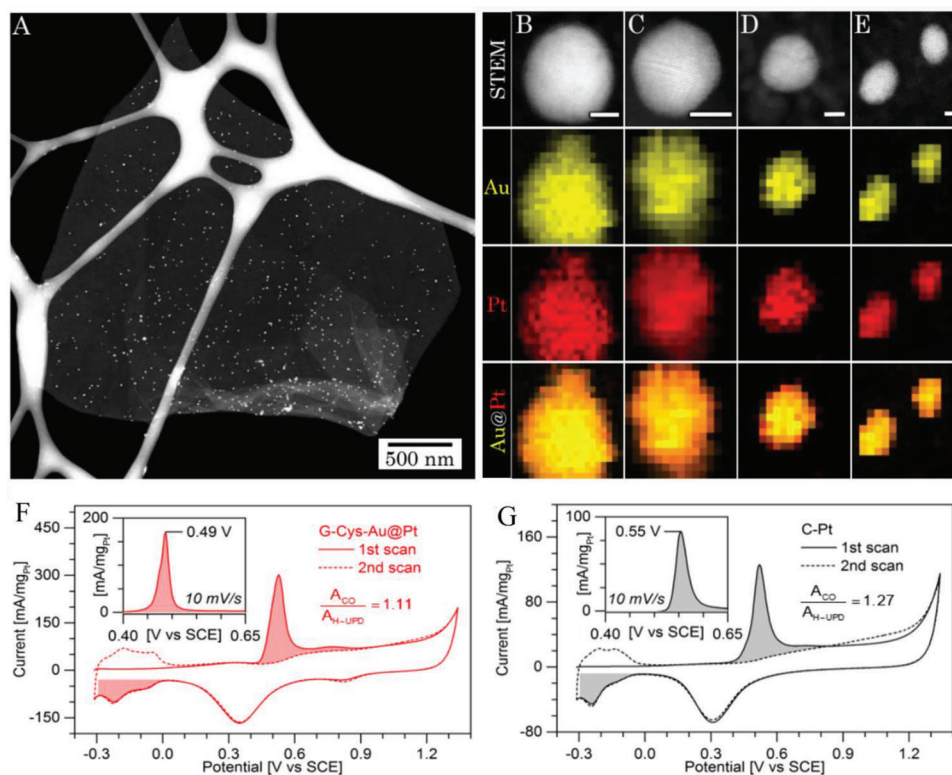
Figure 5. A) STEM image of G-Au@Pt. B–E) HR-STEM images of Au@Pt NPs with corresponding EDX elemental mapping of Au (yellow), Pt (red), and composite images, showing elemental distribution. F,G) CO desorption from CO-saturated Pt surfaces (solid line), and clean, CO-free surfaces (dashed line), for (A) G-Au@Pt and (B) Pt–C catalysts. Reproduced with permission.[138] Copyright 2018, Wiley–VCH.

The chemical NP immobilization at the support enhanced the catalyst stability and its performance by facilitating interfacial electron transfer. The increased activity, and CO poisoning tolerance, compared to non-chemically immobilized G-Au@Pt, and commercial Pt catalyst, was attributed to (1) the tailored electron transfer pathways of covalent bonds integrating Au@Pt NPs into the G framework, and (2) synergetic electronic effects of atomically thin Pt shells on Au cores (Figure 5F,G).

Zhang et al. demonstrated a method for Pt ORR catalyst stabilization against dissolution under potential cycling (a continuing problem in FCVs) by modifying Pt NPs with Au clusters.[139] This behavior was observed under the oxidizing conditions of the ORR, and potential cycling between 0.6 and 1.1 volts for over 30 000 cycles. There were insignificant changes in the activity and surface area of Au-modified Pt catalyst, in contrast to large losses observed with the pure Pt catalyst under the same conditions.

2.3. PGM Ternary Alloys

The research can agree that Pt alloys, more often than not, improve catalytic performance as compared to pure Pt, because the additional metals can change the electronic properties or the Pt surface structure. Although bi-metallic catalysts have garnered great interest and application from both academia and industry, studies have been carried out on polymetallic electrocatalysts to further enhance and/or combat the obstacles of HT-

PEMFC technology.[140–145] The vastness of combinatory possibilities within ternary- and quaternary-alloy catalysis renders them practically unexplored.

Strasser et al. showed that ternary PtRuM (M = Fe, Co, Ni, rhodium (Rh), Ir) had better CO-tolerance than pure Pt, or even PtRu, with superior catalytic activity for methanol oxidation reaction (MOR).[146] This is the key platform for driving the fabrication of ternary catalysts toward improving efficiency at cost reduction. Molybdenum (Mo) is one of the popular elements of interest due to low potential onset for MOR, good CO-tolerance, and the ability to participate in ORR at a FC cathode. CO oxidation is promoted by Mo at low voltages due to the weak bonding to modified Pt surface energy. The two different CO oxidation mechanisms observed in (1) PtRu and (2) PtMo, at different potentials, can exhibit a co-catalytic effect by combining Ru and Mo in a ternary PtRuMo alloy.[147] This was the basis of a study on ternary PtRuMo catalysts, where the electrochemical characterization revealed that all tested ternary catalysts were more active toward CO and methanol oxidation than the binary catalyst. The activity enhancement is associated with a change in the reaction path, via direct fuel oxidation, avoiding the production of CO, due to the synergetic effect of the three metals with the strengthened Mo–Pt and Mo–Ru interactions.

Park et al. studied, PtNiCu ternary catalysts with various compositions for ORR, which were prepared by electrodeposition.[148] The morphologies and crystalline structures were found to depend on the alloy composition. Electrochemical characterization

ADVANCED
SCIENCE NEWS

www.advancedsciencenews.com

ADVANCED
MATERIALS

www.advmat.de
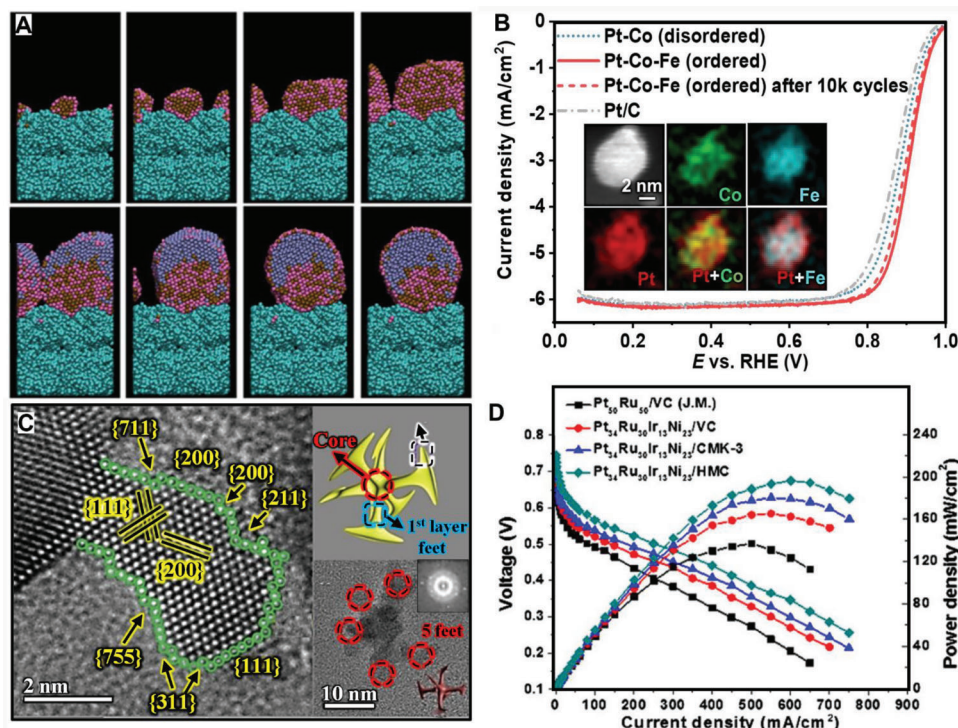
Figure 6. A) Stability simulation snapshots of the deposited core@shell ternary nanocatalyst $Pd_{25}Au_{25}@Pt_{50}$. Reproduced with permission.[149] Copyright 2016, Hydrogen Energy Publications LLC. Published by Elsevier Ltd. B) Low PGM-loaded ternary catalyst performing comparably to Pt–C for ORR. Reproduced under the terms of the Creative Commons CC-BY license.[164] Copyright 2019, The Authors. Licensee MDPI, Basel, Switzerland. C) Novel quaternary hexapod nano-skeletons with HIFs, offering high ORR activity. Reproduced with permission.[160] Copyright 2019, Elsevier B.V. D) The screening and performance of quaternary $Pt_{34}Ru_{30}Ir_{13}Ni_{23}$ catalyst. Reproduced with permission.[162] Copyright 2013, Elsevier Inc.

in the presence of poisoning phosphate anions clearly showed that the PtNiCu catalyst exhibited 5.5-fold higher specific activity than Pt100. The performance of the PtNiCu during the potential cycling in the presence of PA was substantially higher than that of Pt100, suggesting the high resistance of the PtNiCu to phosphate adsorption as well as its superior ORR activity.

Brault et al. conducted a molecular dynamics simulation of FC cathodes based on ternary $Pt_{70}Pd_{15}Au_{15}$ and $Pt_{50}Pd_{25}Au_{25}$ nanocatalysts immobilized on carbon.[149] The Au segregation from the particle bulk to the surface formed a layer of Au coating the cluster surface and a Pt@Pd@Au core-shell structure (**Figure 6**A). For Au content < 25 at%, surface Pt_xPd_y active sites remained available for efficient ORR, as observed experimentally and with DFT calculations.

Zhu et al. made highly active and durable ORR catalysts based on Pd@Pt–Ir nanocrystals with well-controlled facets.[150] With an average of 1.6 atomic layers of a PtIr alloy on the surface, the nanocrystals can be fabricated in cubic, octahedral, and icosahedral shapes. The Pd@Pt–Ir nanocrystals exhibited facet-dependent catalysis, substantially enhanced ORR mass activity (1.88 A mg_{Pt}^{-1} at 0.9 V vs RHE), and durability compared to a commercial Pt catalyst. The Pd@Pt–Ir icosahedra catalyst delivered the best performance of 15 times the commercial catalyst. The DFT calculations attributed the high, facet-dependent activity of the nanocrystals, to easier protonation of O^* and OH^*, relative to the corresponding energetics on clean Pd@Pt surfaces. The DFT calculations also indicated that incorporating Ir atoms

in the Pt lattice destabilized OH–OH surface interactions, thus greatly improving the catalysis and material durability.

As the third alloying element, Fe can weaken the CO adsorption energy on the Pt surface.[151] This occurs due to their respective orbital mixing, where the electron-rich Pt and electron-poor Fe result in hindered electron back-donation from Pt to CO, which weakens the Pt–CO bonding. Another attractive feature of Fe is low-cost precursors compared to Pt and Ru. Due to catalyst stability concerns, PtFe systems can be stabilized by a third element. Often this yields in welcomed increase in mass activity and CO-poisoning inhibition.[152,153] Wang et al. demonstrated a core-shell structured PtFe@PtRuFe nanocatalyst, with an ordered PtFe intermetallic core and a 3–5 atomic-layers-thick PtRuFe shell.[153] The well-defined nanostructure exhibited excellent stability to CO poisoning and resistance to Fe leaching, achieving a factor of 1.68 time enhancement in MOR mass activity compared to the state-of-the-art PtRu catalysts (0.41 mA $µg_{Pt}^{-1}$ at 0.75 V vs RHE). The CO anodic oxidation occurred at much lower potentials (0.39 V vs RHE) than on the commercial PtRu (0.43 V vs RHE) and Pt (0.83 V vs RHE) catalysts.

Ternary catalyst composed of Pt, Ru and Co are considered when trying to minimize CO poisoning and increase performance. A C-PtRuCo trimetallic catalyst was synthesized and applied in a H_2-air FC. The trimetallic catalyst showed robustness to the influence of the air injection into H_2 stream containing CO impurities.[154] Semasko et al. prepared G-immobilized PtRuCo NP catalyst with different molar ratios, by microwave-assisted

process. The material with Pt:Ru:Co molar ratio of 3.5:1:23 had the highest activity for electrooxidation of methanol fuel.[155]

Ternary PtRuNi alloys have also attracted attention for catalytic abilities, coupled with high poisoning tolerances. Liang et al. prepared a carbon-supported PtRuNi NPs via a microwave-assisted polyol process, and the nanocomposite exhibited an enhanced tolerance to CO.[156] The improved performance was related to the H_2 spill-over on the catalyst surface composed of the high proton- and electronic-conducting Ni hydroxides, which enhanced the oxidation of CO_{ads}. Almeida et al. prepared PtRhNi nanocatalyst by wet chemistry and studied electrooxidation of ethanol. The X-ray diffraction analysis revealed distortions in the Pt lattice caused by the different atomic radii of Rh and Ni in the structures of PtRh and PtRhNi catalysts. They found that the oxidation reaction pathway selectivity closely depended on the surface composition of the catalyst.[157] The fuel oxidation selectivity can, therefore, be fine-tuned via optimizing the elemental ratio of metals during the catalyst synthesis.

The improvement in the durability of octahedral PtNi can be achieved by introducing a cheaper alloying element than Ru, such as Mo or Cu.[116,158] Dionigi et al. reported high ORR catalytic activities of Mo-doped octahedrally shaped PtNi NPs on a MEA level (0.45 A mg_{Pt}^{-1} at 0.9 V_{cell}), Figure 3C.[116] They succeeded to realize a high Ni retention even after prolonged potential-cycling tests. Stability losses were mainly attributed to the loss of the octahedral NP shape, demonstrating how Mo atoms on the surface impact the Ni surface composition, which then gives rise to the exceptionally high experimental ORR activity.

Han et al. synthesized hollow and porous PtRhCu trimetallic nanoboxes (CNBs) with a tunable Pt:Rh atomic ratios, which exhibited morphology and composition-dependent electrocatalytic activity. The introduction of Cu inhibited the CO-poisoning, while Rh elevated the stability of PtRhCu CNBs.[158]

Nan et al. investigated PdM core with Pt atomic-thin shell catalysts (M = Ni, Co, and Fe). PdFe@Pt exhibited the best ORR performance (0.88 mA cm^{-2} and 1.14 A mg_{Pt}^{-1} at 0.9 V vs RHE)—5.4 times more than the commercial Pt catalyst.[142] A ternary alloys of exclusively noble metals Pt, Pd, and Rh was investigated by Vedyagin et al.[159] They report that the metals ratio played an important role in determining the catalytic activities and their thermal stabilities. For most reported alloy catalysts, an improvement due to alloying was reported.

2.4. PGM Quaternary Alloys

Among various catalyst compositions, binary and ternary Pt-based catalysts have been broadly investigated in recent years, showing enhanced catalysis, stability, and anti-poisoning ability compared to commercial carbon-supported Pt catalyst. Increasing number of researchers are, however, studying the quaternary Pt-based catalysts and their applications in electrocatalysis. The motivation behind it is in Pt-reduction, while increasing the catalyst activity. By alloying the NPs, the catalysis, poisoning, stability, and reaction selectivity can be fine-tuned to a great extent. When alloyed with, for example, transition metals, the usage of Pt can be significantly reduced, while preserving catalyst activity (Figure 6B). These high-efficiency catalysts are mainly hollow spheres, nano-frames and nano-skeletons, that is, a highly open

structures with efficient atomic utilization, where electron transfer and mass exchange are greatly accelerated.

Huang et. al reported a novel synthesis of quaternary hexapod nano-skeletons with HIFs, composed of core, first-layer, and second-layer feet (Figure 6C).[160] These vertex-reinforced PtCoNiMo hexapod nano-skeletons exhibited enhanced mass activity, stability, and anti-poisoning ability toward MOR and ORR, compared to commercial Pt catalyst.

Li et al. synthesized quaternary PtPdNiP mesoporous nanospheres (PtPdNiP MNs) using a facile two-step strategy.[161] The as-fabricated PtPdNiP MNs exhibited superior catalytic activity and durability for the ORR due to mesoporous nanoarchitectures and elemental composition effect. The proposed synthetic strategy is highly feasible for the fabrication of metal–nonmetal nanoarchitectures with controlled compositions.

Kim et al. reported PtRuIrNi catalyst study by a robotic dispenser and combinatorial optical screening method (Figure 6D).[162] A quaternary catalyst with $Pt_{34}Ru_{30}Ir_{13}Ni_{23}$ composition is found to be the most active, demonstrating superior electrochemical activity and stability for MOR compared to commercial Pt_{50}–Ru_{50} binary catalyst. The in-study-developed carbon-supported PtRuIrNi, and hierarchical carbon-supported PtRuIrNi catalysts showed activity enhancements of ≈ 26–50%, while demonstrating better stability. The improvement in catalytic activity is attributed to a new active quaternary composition, the activity of which can be explained by a bifunctional mechanism: (1) electronic effect, and (2) stability effect occurring from addition of Ni and Ir. Huh et al. reported a synthesis of N-doped G-supported quaternary electrocatalyst NG-PtRuFeCo, which was evaluated for ORR and MOR in a FC.[163] The catalyst exhibited excellent CO tolerance, lower onset potential, and direct ORR reaction pathway. The N-doping and synergetic effects of alloying low-cost Fe and Co with Pt and Ru makes NG-PtRuFeCo an excellent bifunctional catalyst.

The progress in quaternary electrocatalyst research has a high future promise in terms of catalyst mass activity and durability. The attractive perspective is the fine-tuning catalyst features to best address a particular application since each of the alloying elements contributes with its own inherent properties. This is where simulations and DFT can help predict catalyst behaviors, which eventually need to be experimentally confirmed. The processing of these complex systems needs to be cost-effective to be widely applied within the field, especially in commercial systems.

3. PGM-Free Catalysts

PGM-free catalysts are an attractive alternative to PGMs in the PEMFC due to potential cost lowering.[165] Focus is placed on cathode electrode requirements, where the demand for Pt is substantial to minimize ORR kinetic losses. In their most active form, PGM-free catalysts present catalytic sites scaled down to the atomic level.[165,166] Developing single-atom catalysts (SACs) can be employed as a strategy to (1) improve the catalyst metal content utilization, and (2) help to increase active site density needed to match the activity of PGM catalysts. In acid, the most active subgroup of PGM-free catalysts is the single-atom transition metal N-doped catalysts (M–N–C), where Pt is replaced with lower-cost earth-abundant metals such as Fe, Cu,

2302207 (13 of 28)

ADVANCED
SCIENCE NEWS

www.advancedsciencenews.com

ADVANCED
MATERIALS

www.advmat.de

Ni, Co, Mn, and Sn.[167,168] Among M–N–C, the active center of Fe–N–C, primarily the atomic FeN_4 moieties, is theoretically predicted and experimentally verified as the most active site for the ORR in acidic electrolytes.[169] One or multiple-step pyrolytic methods have been used to produce single atom Fe–N–C utilizing the functionalities of metal organic frameworks (MOFs).[170] In terms of synthesis, the large surface energy of single metal atoms induces aggregation resulting in the formation of metal NPs during pyrolysis.[171] Although metal NP encapsulation in graphitic carbon is shown to have a protective role toward demetallation,[172,165] thereby enhancing stability,[172,165] aggregation is an undesirable trait as it limits load of active metal on the C network, suppressing active site formation. Hence, due to the competition of metal-N binding by metal atom aggregation, metal loadings are typically kept < 1–2 wt%, which can limit the activity of M–N–C catalysts.[173,174]

To enhance FC performance, PEM FC MEAs possessing M–N–C coated cathodes are usually operated under fuel and oxidant over-pressures. Typically, the performance of LT-PEMFC with PGM-free electrodes (e.g., Fe–N–C, Co–N–C, and Mn–N–C cathodes) often degrades in power density by 40–80% within 100 h operation under 2.5 bar H_2/O_2 constant voltage (e.g., 0.5V) conditions.[175] This substantial loss in current density is attributed to the rapid deactivation of M–N–C active sites. Efforts on improving durability by regulating the M–N–C coordination structure led to a Fe–N–C voltage retention up to 80% after 30h of LT-PEM FC operation at constant voltage (0.5V) under 0.5 bar H_2/O_2.[176] Demetallation, carbon corrosion, poisoning of active sites and micropore flooding are proposed mechanisms for the fast deactivation of M–N–C in acid conditions.[167,177,178]

An interesting feature of Fe–N–C is that they exhibit better ex situ ORR activities in PA electrolyte, which indicates promising application for HT-PEMFC.[179] The adsorption of PA anions is negligible on PGM-free catalysts, while Pt-derived catalysts suffer from this.[36] Although the peak power density is significantly lower than that of Pt/C under HT-PEM at the typical operating temperature of 160°C,[180] G-based Fe–N–C outperformed Pt/C at elevated temperature (230°C), showing stability and tolerance to phosphate poisoning.[180] Similarly, atomically dispersed FeCu (4:1) bimetallic cathode catalysts have delivered HT-PEM power density comparable to that of Pt/C (1 mg_{Pt} cm^{-2}) at 230°C.[181] Stability test (hold at 0.5V) at elevated temperature (230°C) revealed better current retention than that of Pt/C over 100h.[181]

Regarding operation at 160°C, an activity enhancement for Fe–N–C was obtained by neighboring Fe–N_4 sites with phosphorus (P). The charge density and phosphate poisoning tolerance of Fe–N_4 was found to increase after regulating the structure of the single atom site via P-doping.[182] The catalyst outperformed commercial Pt/C in HT-PEM (160°C), delivering exceptionally high power density.[182]

Although Fe–N–C delivers considerably higher current density under LT-PEM (80°C) than HT-PEM (tested at 150°C),[183] Fe–N–C cathodes operated for HT-PEM show improved stability. A 34% voltage loss at 100 mA cm^{-2} for 400 h has been demonstrated for a Fe–N–C cathode operated for HT-PEM (160°C).[179] Degradation is attributed to loss of ECSA or/and acid flooding in the electrode.[179] Thereby, a retention of up to 66% in voltage, being in the same range for other Fe–N–C tested in HT-

PEMFCs,[184] ranks higher than most Fe–N–C cathodes operated for LT-PEM.[175,185,186]

Fe–N–C shows the most comparable SAC ORR activity to commercial Pt–C in acid,[187] but their HT-PEMFC application has been limited due to their lower volumetric activity. Fe–N–C electrodes are ≈ 5–10 times thicker than Pt–C catalyst layers,[188] to compensate for the decreased intrinsic performance toward the ORR. This thickness increase inhibits mass transport by occupying a higher total electrode volume but also adds more electric resistance to the cell. Ideally, the thickness should not exceed 10 μm to minimize mass transport issues.[188]

Compared to Pt–C and PtCo–C MEA tests, 2.5 times larger ORR and mass transport resistances were demonstrated for Fe–N–C CLs.[60] This is attributed to Fe–N_x active sites being located dominantly in the nanometer-scaled pores, exhibiting a substantial mass transport resistance.[60] Evaluation of Fe–N–C performance under HT-PEM fuel cells have shown a clear dependency on backpressure, highlighting the importance of efficient mass transport.[189] As the activity of single-atom Fe–N_x catalytic sites is crucial for high performance, the impact of the morphology and nano-design is even more relevant in this type of catalyst.[60]

There are still prominent application-based challenges that Fe–N–C catalysts need to overcome for HT-PEMFC. Progress must be made in maximizing the number of electrochemically accessible active sites, increasing the TPB. The Fe–N–C structure consists of meso (2–50 nm) and microporous (< 2 nm) network, where in-plane defects easily inhibit active site utilization.[190,191] Proton transport is negligeable in the smallest porosities since Fe–N–C catalysts experience slow conditioning as they require the PA to access not only small mesopores, but also active sites hosted in the micropores.[60] CL design needs to be explored further for Fe–N–C utilization in HT-PEMFC. The strong impact of Fe–N–C properties like hydrophilicity and acid distribution are shown to influence the FC performance.[192] Furthermore, a more reliable testing methodology needs to be established for ex situ CL testing results to be transferable to MEA level.[192]

4. Catalyst Support Materials

It is important to note that catalyst supports play a major role in the performance of catalysts and the transfer of fuel and charge in FC systems. As a result of support, catalyst NP dispersion, stability, and utilization are affected, which is reflected in catalyst particle sizes, their distributions, and degree of alloying. The support governs the mass transfer in MEAs by controlling the contact between reactants and CL active sites,[193–195] therefore, it plays a significant role in catalytic activity, cost, performance, and durability.[196,197] Carbon (C) is generally used as a supporting material for Pt-based NPs in HT-PEMFC, but C can be electrochemically oxidized under harsh operating conditions, resulting in NP detachment and performance loss. Chemical degradation of the support material in HT-PEMFC is faster, compared to LT-PEMFC, due to the higher operating temperature and the presence of concentrated PA.[31,44] Much effort has been devoted to developing durable catalyst support materials. The adhesion of PGM-based catalyst particles to the supporting layer is crucial

**ADVANCED
SCIENCE NEWS**

www.advancedsciencenews.com

**ADVANCED
MATERIALS**

www.advmat.de

Table 2. Summary of the physical characterization of various carbon blacks.

Carbon blacks	Type	Surface area [m² g⁻¹]	Particle size [nm]
Denka black	AB	58	40
Shavinigan	AB	70–90	40–50
Conductex 975	FB	250	24
Vulcan XC-72R	FB	254	30
Black pearls 2000	FB	1475	15
3950	FB	1500	16
Ketjen EC 300J	FB	800	39
Ketjen EC 600JD	FB	1270	34

to ensure catalyst durability. Additionally, support material can influence the density of states in the metal d-band, due to the electrical connection between the support and the catalyst NPs. Researchers are, therefore, continuously working on designing high-efficiency electrocatalysts by employing novel support materials. Some of the representative work and recent support material development are summarized here.

4.1. Carbon Black

The graphite-like, mesoporous characteristics of carbon black (CB) have made it a common choice among carbon supports.[198,199] PEMFCs typically use Vulcan XC-72, Black Pearls 2000, Ketjen EC 300J, and Ketjen EC 600JD carbon support materials, all of which are high surface-area materials (>100 m² g⁻¹) with good electrical conductivity. CB is further classified as: acetylene black (AB) and oil-furnace black (FB).[200,201] **Table 2** summarizes the physical characterization of different carbon blacks.[202] There have also been a variety of catalyst supports developed over the years such as carbon nanotubes (CNTs),[203,204] carbon nanofibers (CNF),[205]

4.2. Graphitized Carbon Black

Graphitized carbon black (GCB) is another high surface area material obtained by recrystallizing CB at 2500–3000°C in an inert atmosphere, to obtain well-ordered, crystalline domains. The surface area generally achieved is in the range of 100–300 m² g⁻¹.[206] Graphitization affects the physical and electrical properties of carbon materials,[207] as evidenced by increased durability observed in C-based substances as their graphitization level rises.[208] Selvaganesh et al. demonstrated higher stability of GCB support than for C.[209] The performance of Pt NPs immobilized on non-GCB support cathode was found to have deteriorated by 54%, while the performance of Pt NPs on GCB deteriorated by 24% during 8000 potential cycles.

4.3. Carbon Nanotubes

Due to excellent electrical conductivity, mechanical robustness, and higher durability, CNTs are attractive catalyst support.[210,211]

Wildgoose and Lee et al. synthesized Pt-decorated carbon nanotubes (Pt-CNTs) for PEMFCs.[212,213] According to Matsumoto et al.,[214] CNT with 40 wt% Pt outperformed commercially available C-Pt catalyst. Girishkumar et al.[215] demonstrated that single-walled CNTs (SWCNT) may be an excellent Pt NP support material when compared to commercial CB support. As a result, studies have been conducted to increase the efficiency of Pt via unique properties of CNTs. Although widely used as metal catalyst supports for PEMFCs due to their unique properties,[216] the CNT surface is inert and incompatible with metal NPs. Unfunctionalized CNTs with high Pt loadings tend to aggregate.[217] Functionalization of CNTs is, therefore, a primary requirement in immobilizing catalyst NPs. Acid activation, high-temperature potassium hydroxide (KOH) activation, and annealing (graphitization) can improve the anchoring properties of CNTs.[218] Okamoto et al. synthesized the PBI-wrapped multi-walled CNT (PBI/MWCNT) support for subsequent deposition of Pt NPs, creating Pt-PBI/MWCNTs. They discovered the deposited Pt NPs had a higher electrochemical utilization efficiency than when on pristine MWCNT surfaces.[219]

The anode HT-PEMFC catalyst has been made using carbon nanotubes pyridine (Py)-functionalized CNTs. The excellent electrochemical contact between the CL and the PA allowed these catalysts to work incredibly well under reformate conditions, due to Py groups that engage with the PA.[220] Fujigaya et al. used a high-resolution transmission electron microscope (HR-TEM) to study the immobilized Pt NPs on pyridine (Py) PBI-wrapped MWCNTs (Pt-PyPBI/CNTs). The NPs were in close contact with the MWCNT surfaces, being partially exposed from the PyPBI film layer, forming good TPB conditions, crucial for high electrocatalysis.[221] Pt NPs deposited on PyPBI/CNT showed increased durability than when deposited on PyPBI/CB, according to Berber et al.[222] Yu et al. investigated the use of PBI and Py-meta-PBIs (Py-m-PBI) as CNT wrapping polymers to immobilize Pt NPs, resulting in Pt-PyPBI/CNT catalysts for HT-PEMFCs.[223] The best performance was achieved with PyPBI-wrapped CNTs with Pt loading of 44 wt.% and NP size of 3.3 nm.[224] Eren et al. synthesized Pt-PBI/MWCN, showing significantly higher durability than the commercial Pt–C, retaining over 80% of its maximum ECSA after the 1000 potential cycles.[225] The behavior of Pt-PBI/MWCNT has been evaluated in a MEA, at four different temperatures. During the single-cell operation at lower temperatures, the CNT-covering polymer film blocked some of the catalytic sites of the framework. In contrast to commercial Pt–C, the peak power density of Pt-PBI/MWCNT slightly increased from 38 to 47 mW cm⁻² (at 95 and 117 mA cm⁻²) while increasing the temperature from 150 to 180 °C. This indicated that the Pt-PBI/MWCNT may be a better candidate at higher operating temperatures (>170 °C) due to the increase in conductivity of PBI.

In comparison to CNTs, graphitized MMCNTs (GCNT) possess higher electrochemical resistance.[226] The GCNT, CNT, and C support materials were evaluated by electrochemical ex situ and in situ measurements, in HT-PEMFC.[227] The accelerated stress test (AST) with the triangle-wave protocol showed the Pt-GCNT catalyst had higher electric resistance compared to Pt-CNT and Pt–C catalysts, however, GCNT-supported Pt NPs showed the highest metal utilization efficiency, stability, and HT-PEMFC performance among the tested C support.

**ADVANCED
SCIENCE NEWS**

www.advancedsciencenews.com

**ADVANCED
MATERIALS**

www.advmat.de
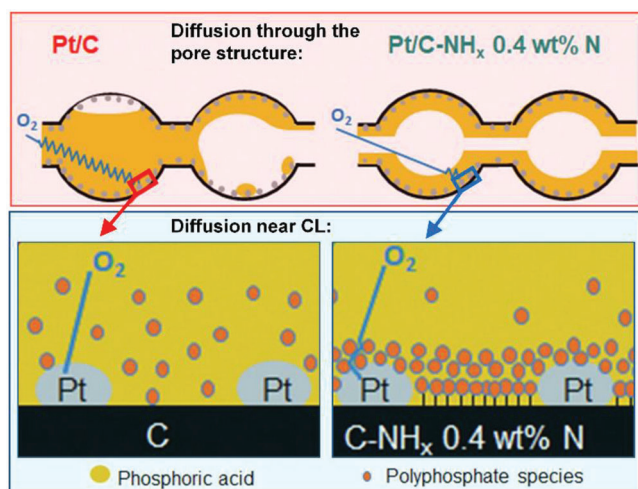
Figure 7. Oxygen diffusion through PA in the pore structure for Pt/C and NHx 0.4%. Reproduced with permission.[229] Copyright 2021, Elsevier.

4.4. Nitrogen-Functionalized Supports

Nitrogen (N)-functionalized catalysts have been used in LT and HT-PEMFCs to improve the ionomer and PA distribution in the CLs. Carbon functionalized with N groups (mainly amide, imide, and lactam) was employed as the catalyst support material in conventional PEMFCs. The coulombic interaction of the N groups and the sulfonate anions of the ionomer resulted in formation of uniformly dispersed ionomer coatings over the CL, with increased performance due to improved oxygen mass transport.[228]

Carbon support materials with N sites exhibit great stability in HT-PEMFCs. The N groups create a PA network across the CL due to the acid–base chemistry. The low-functionalized N-modified catalyst usually has lowered mass transport (the oxygen diffusion in the macrostructure), but increased ORR resistance (reaction resistance and oxygen diffusion in the vicinity of the catalyst). The enhanced mass transportation, however, prevails and enhances the overall performance. Because these electrodes absorb more acid than the non-functionalized reference catalyst, the amount of acid given to the MEA must be carefully assessed when utilizing functionalized catalysts. Pimperi et al. studied MEA performance, kinetics, and transport-related voltage losses of N-modified carbon supports in the CL of a HT-PEMFC.[229] They demonstrated that even modest moieties of N-containing functional groups enhanced performance due to the increased dispersion of PA in the CL (**Figure 7**). Although this strategy can successfully manage the PA distribution, it needs to be optimized for extended MEA operation times.

4.5. Graphene, Graphene Oxide, and Reduced Graphene Oxide

The advanced nanostructures of graphene (G) materials have attracted researchers' attention, as potentially an excellent catalyst support material, due to unique physical properties, for example, excellent electrical conductivity, large specific surface area, high thermal conductivity, high mechanical strength, and good chemical stability.[230]

The performance of Pt NPs immobilized on G nanoplatelets (GNP) showed superior performance than Pt NP immobilized on graphene oxide (GO) and Pt–C in HT-PEMFC.[197]

A new generation of catalysts with improved (1) electrocatalytic activity, and resistances toward (2) poisoning, and (3) carbon corrosion, is expected from Pt–G.[138,231] Recently, Holmes et al. prepared single-layer graphene (SLG) on electrode surfaces to increase TPBs by managing PA around CLs (**Figure 8**) and studied its effect on performance and durability of PBI membranes in HT-PEMFCs.[232]

The MEA durability in the AST has been significantly increased by the SLG. The pure PBI membrane-based MEA exhibited a considerable performance decline over time due to the increased PA leaching at the TPB, brought on by the high acid doping level (ADL) in the PBI. Cathodic SGL resulted in a peak power density of 365 mW cm^{-2} at 0.4 V$_{cell}$ and 150 °C, a substantial increase over MEA without the SGL.[232] Nevertheless, this material is unlikely to be practically applied in commercial systems due to its complex preparation process and high cost.

The main reason why G, a pure catalyst support material, is unable to perform well in fuel cells is because of the 2D structural stacking, which effectively covers large Pt active areas and, therefore, limits gas diffusion, especially at high current densities.[233] Doping is a useful technique for altering the characteristics of C materials for use in a variety of energy conversion devices.[234]

4.6. Composite Supports

The Pt NPs supported on N-doped, electrochemically reduced exfoliated GO with intercalated CB (Pt-NrEGO/CB) has been prepared. The function of this composite catalyst support was to serve as a 3D physical barrier inhibiting the leaching of platinum by graphene flakes, resulting in enhanced gas transport. The N-doped sites improve Pt NP anchoring and inhibit C corrosion, therefore, the composite catalyst was first applied in LT-PEMFCs, showing good performance and stability.[235] The performance and durability in HT-PEMFCs were also improved with Pt-NrEGO/CB, despite the reduced Pt loading.[236] Pt-NrEGO/CB prevented the agglomeration of Pt NPs via strong bonding between Pt and N sites, resulting in Pt mean NP size of 5.5 nm as opposed to 6.8 nm in Pt–C. The Pt–C ECSA decreases by 97.99%, while Pt-NrEGO/CB's by 13.65%, after the AST. The NrEGO flakes served as PA redistribution barriers, which enhanced the extent of TPBs, resulting in stable operation with a low decay rate of 20 μV h^{-1} within 100 h of testing. The Pt-NrEGO/CB reached a maximum power density of 0.411 W cm^{-2} at 0.591 V$_{cell}$ (0.25 mg$_{Pt}$ cm^{-2}) in HT-PEMFC, which was three times that of commercial Pt–C (0.134 W cm^{-2}). The Pt-NrEGO/CB electrode resistance (0.560 Ω cm^2) was lower than for the Pt–C electrode (0.728 Ω cm^2), after the AST protocol.

Furthermore, NrEGO/CB is more cost-effective than SLG placed on the CL surface to stop PA loss. Comparatively speaking, spraying the Pt-NrEGO/CB CL in industrial production is simpler than the additional wet transfer step required for SLG material.

The increased catalyst durability has been demonstrated in HT-PEMFC by using graphitic carbon nitride (gC$_3$N$_4$) nanosheets and acid-treated CB as support material for Pt

ADVANCED
SCIENCE NEWS
www.advancedsciencenews.com

ADVANCED
MATERIALS
www.advmat.de
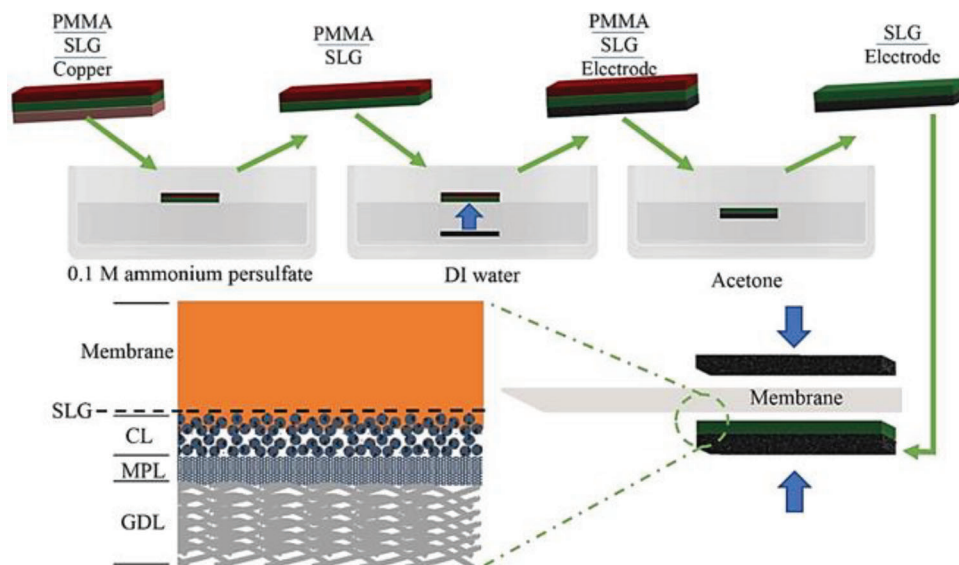
Figure 8. The transfer of SLG and the structure of membrane-electrode-assembly. Reproduced with permission.[232] Copyright 2021, Elsevier.

NPs.[237] The support assisted in formation of small Pt NPs (1.8 nm) on gC_3N_4 nanosheets, as shown by TEM imaging. The Pt-gC_3N_4-C ECSA was 87.6% preserved after an AST protocol of 5000 cycles, significantly better result than for commercial Pt–C (54%). A preliminary HT-PEMFC100-hour durability test showed no discernible decline in voltage for MEA using Pt-gC_3N_4-C as the cathode electrocatalyst, while Pt–C MEA exhibited 91 µV h^{-1} voltage degradation rate. The robust durability of Pt/gC_3N_4-C is attributed to (1) the excellent stability of gC_3N_4 nanosheets, (2) the spatial confinement of CB to Pt NPs, and (3) the strong bond between Pt and gC_3N_4 nanosheets.

4.7. Metal Oxides

Some research has been done on increasing the catalyst stability by incorporating metal oxide supports. Ignaszak et al. studied the stability of TiC and core-shelled TiC@TiO_2 as catalyst supports.[238] The ECSA loss was 78% for Pt–Ti, and 94% for Pt_3Pd–TiC after only 500 cycles. The degradation in TiC-supported catalysts was much faster than for commercial carbon support.[239] The core-shell Pt_3Pd/TiC@TiO_2 catalyst, however, showed significantly improved electrochemical stability compared to TiC-supported catalysts.[240] Lobato et al. tested SiC-based catalyst supports in MEA operating at 160 °C.[239] After the test, they observed that the aggregated Pt NP size increased the FC stability while decreasing the ECSA and system performance.[241] The metal oxide supports suffer from poor inherent conductivity, which makes it necessary to develop different strategies to increase it. Furthermore, being generally unstable under elevated temperatures and highly acidic conditions, metal oxides do not seem to be promising catalyst support materials in HT-PEMFC.

5. Catalyst Degradation

Pt and its alloys are generally used catalysts for HT-PEMFCs. The durability of PGM-free cathode catalysts is to a certain extent limited. Issues arise from single-atom metal leaching and carbon corrosion.[242] Decomposition of Fe–N_4 due to the weakening of Fe–N bonds may occur from operation-driven Fe oxidation. Carbon corrosion weakens N–C bonds which further destabilizes Fe–N_4, particularly impactful at high voltages (> 0.7V).[192] Under such conditions, Fe atoms can cluster to form particles, triggering a loss of ECSA.[243] In addition, peroxide-related radicals form at the CL/membrane interface and accelerate the degradation of active sites and adjacent carbon structures at low operating voltages (< 0.5V).[192] When the operating temperature increases, H_2O_2 can easily decompose[244] making Fe oxidation less prominent for HT-PEMFCs. A further loss of Fe active centers relates to the presence of water flux in the Fe–N–C micropores,[245] which is not as common at temperatures equal to and > 160°C.[182] Instead, PA flooding can limit gas diffusion. Over time, it renders sites inactive due to the low solubility and diffusivity of oxygen in PA.[246] Sites that are partially covered in PA are less challenged to form TPBs than sites with full PA coverage.[247] High mass transport resistances attributed to low gas diffusivity within hard-to-access Fe–N–C micropores are previously reported for HT-PEMFC.[60] This is indeed one of the key Fe–N–C challenges in HT-PEMFCs.

The degradation mechanisms of HT-PEMFCs for Pt and Pt-based alloys are similar to the ones in LT-PEMFCs, with additional complexities arising from higher operating temperatures and presence of PA.[248,249] The acidic HT-PEMFCs environment[44,248,250] enables the precipitation of the dissolved Pt in the membrane, at the nano- and atomic-scale by Pt ion reduction. This phenomenon is confirmed by TEM analysis. Furthermore, the elevated operating temperature weakens the binding energies of Pt NPs to the C support due to a higher progression of C corrosion.[44,248,251]Corrosion of the catalyst support results

**ADVANCED
SCIENCE NEWS**

www.advancedsciencenews.com

**ADVANCED
MATERIALS**

www.advmat.de
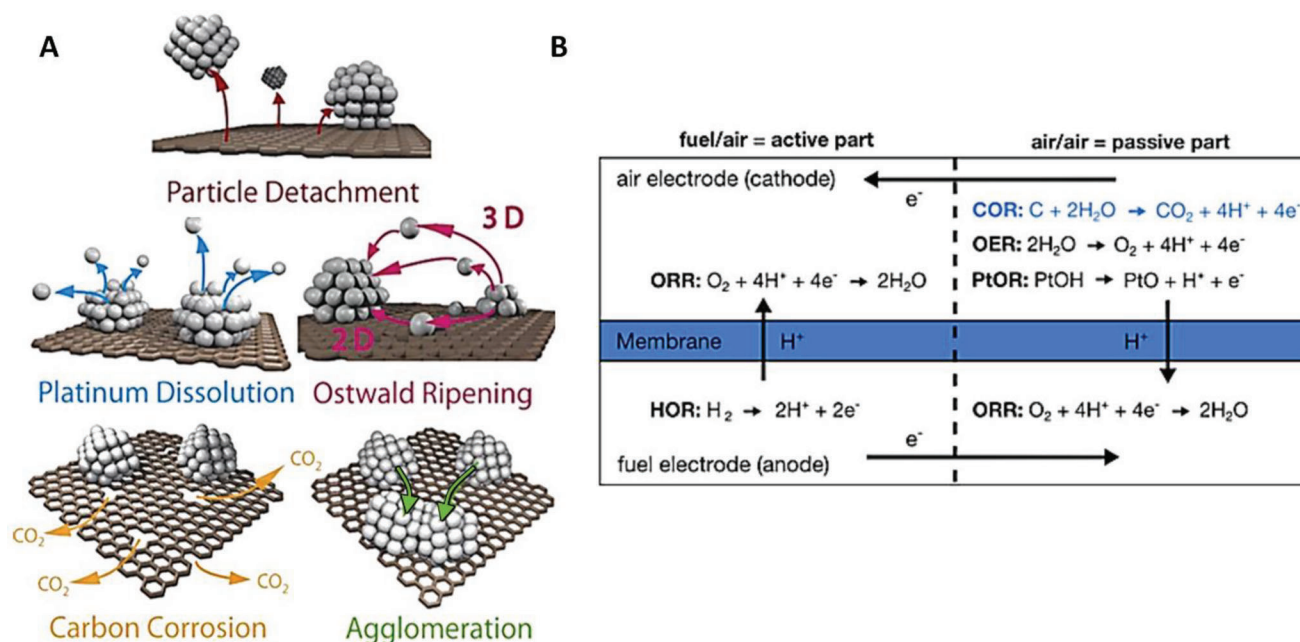
Figure 9. A) Four mechanisms for Pt particle growth in fuel cells. Reproduced under the terms of the Creative Commons CC-BY license.[265] Copyright 2014, The Authors. Licensee Beilstein-Institut. B) Reverse-current decay mechanism, which explains the carbon oxidation reaction at the air electrode during a gas feed exchange at the fuel electrode. Reproduced with permission.[263] Copyright 2016, Wiley–VCH.

in (1) ECSA loss due to particle detachment, (2) loss of C electrical conductivity, and (3) increased mass transport resistance, due to pore narrowing by the oxides formation.[252]

The four mechanisms that irreversibly degrade the catalyst ECSA are (1) carbon corrosion, resulting in NP agglomeration or detachment, (2) NP coarsening via the Ostwald ripening, (3) Pt dissolution which ends up in recrystallization in the electrolyte matrix, and (4) NP coalescence, occurring due to mobility of Pt crystallites on the carbon surface (**Figure 9**A).[253,254] The way of quantifying the Pt degradation is by NP agglomeration, particle isolation, and dissolution. The dissolution of the small Pt NPs occurs in metallic (Pt^0), ionic (Pt^{2+}), or both forms, when exposed to high operating cathodic potentials, especially under OCV conditions, according to the following reactions:[255]

$$Pt \rightarrow Pt^{2+} + 2e^- \tag{4}$$

$$Pt + H_2O \rightarrow PtO + 2H^+ + 2e^- \tag{5}$$

$$PtO + 2H^+ \rightarrow Pt^{2+} + H_2O \tag{6}$$
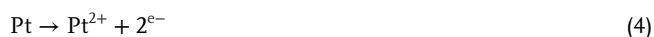
As reported by Yousfi–Steiner et al., the main degradation mechanism associated with long-term MEA operation is the constant decrease of ECSA, which is mostly connected to Pt dissolution, migration, and reprecipitation.[253] It has been demonstrated that growth of Pt NP size at the cathode occurs faster than at the anode due to the higher cathodic potentials.[44] Yu et al.[254] studied relation between initial NP size and various degradation mechanisms, concluding Pt dissolution was the predominant degradation mechanism. They also observed the increase of coalescence with smaller particle sizes. Shao–Horn et al. claimed that initially,

smaller particle sizes accelerated the dissolution rate and solubility, therefore, progressively losing ECSA due to the higher Gibbs free energy of the smaller particles.[45,256] Additionally, ECSA decreases due to the operation-specific harsh conditions in HT-PEMFC. Recently, Vega Paredes et al.[257] studied long-term operation degradation (12 000 h) at 0.2 A cm^{-2} and 160 °C, in a HT-PEMFC stack. They found two operation-related degradation mechanisms, (1) thinning of the functional layers as well as Kerr et al.,[249] and (2) dissolved catalyst redistribution within the MEA.

It has been reported that C corrosion significantly contributes to the catalyst degradation,[258,259] when exposing the cell to high cathodic potentials (> 0.6 V vs RHE), furthermore Pt dissolution rate increases by 9 orders of magnitude when the potential is swept from 0.6 to 1.0V versus RHE.[260] Bandlamudi et al. demonstrated that C in the CL degraded at high potentials by measuring the CO_2 emitted from the cathode. The CO_2 concentration monotonically increased with the applied potential.[261] Borup et al. showed that cathode particle growth increased with rising potential during AST protocols.[256]

Søndergaard et al. demonstrated that humidification exacerbates the detrimental effect of potential cycling on the Pt catalyst durability, acting as an AST stressor.[262] Borup et al. stated that Pt particle growth slows down with decreasing relative humidity.[256] Bandlamudi et al. demonstrated the dependance of humidity to the reaction products in a carbon corrosion test where the cell potential was held at 1.2V.[261] The CO_2 concentration rose by up to 4 times with the increase in reactant gas humidity, when compared to non-humidified gas flows.

Even under steady-state operating conditions, C is beyond its thermodynamic stability limits at the cathode. The C oxidation reaction under those conditions (when cathode potential is < 1.0

Table 3. PEM failures linked to catalyst degradation.[253].

Issue	Potential cause	Indication
Pt dissolution and agglomeration-	–Starvation	–Loss of the catalytic active surface
	–Ageing	–Presence of catalyst particles in the exhaust water
	–Cycling	–Increase in particles size
	–Fuel and oxidant starvation:	–Uneven current distribution (negative values)
	–Flooding, uneven reactants supply	–Observation of temperature distribution
	–GDL or flow channel obstruction.	–Increase of each cell voltages dispersion and negative values
	–Cycling conditions (cathode)	–Inversed flow at the fuel outlet
	–Start–up/shutdown (anode)	–Detect C, CO, and CO_2 at the exhaust
	–Flooding	–Uneven current distribution (negative values)
	–Insufficient reactants supply	–Observation of temperature distribution
	–Uneven reactants supply (GDL or flow channels obstruction)	–Dispersion of individual cell voltage
		–Increase of the individual cell voltages dispersion and including negative values
Carbon corrosion		–Inversed flow at the fuel outlet
Starvation		–Presence of "Vacuum effect"

V) is negligible due to the sluggish reaction rate.[261,263] Above 1.0 V, however, C can severely corrode (Equation 4), resulting in irreversible performance degradation (Figure 9B).[261]

$$C + 2H_2O \rightarrow CO_2 + 4H^+ + 4e^-, E° = 0.207 \text{ V versus SHE} \quad (7)$$
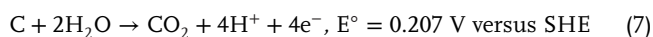
The C corrosion is affected by temperature, relative humidity, cell potential (e.g., OCV conditions), start-stop cycling, and fuel starvation.[261] These phenomena are only accelerated in the presence of Pt. The structure of the C support also influences the degradation rate. An amorphous material with a higher specific surface area is more prone to oxidation than the crystalline counterpart with a smaller specific surface area. The highly graphitized C supports show excellent resilience to oxidation, at the detriment of anchoring sites.[264]

Catalyst degradation is further accelerated by FC dynamic operation, for example, start-stop cycling where cathodic carbon corrosion is accelerated by the so-called reverse current effect. When starting up the fuel flow after a system shutdown, the anode gas can get mixed with the air that has diffused into the anode compartment. This creates high cathodic transient potentials of up to 1.6 V, causing C corrosion and consequently irreversible damage to the fuel cell (reverse-current decay mechanism).[261,263,266] Other dynamic operation protocols in fuel cells can accelerate catalyst degradation, like load cycling[252] which exposes the cell to the severe corrosion of C supports, especially when cycling near or at OCV values.[267] Due to the thermal expansion/contraction of the electrodes, at different degrees of hydration, thermal cycling can cause severe C corrosion and metal particle sintering.[15] Consequently, catalyst area loss inhibits the ongoing electrochemical reactions, which has a detrimental effect on the FC performance.

One of the most common causes of FC failure is MEA starvation—a FC activity at sub-stoichiometric reactant conditions.[268] The CL is degraded severely under HT-PEMFC starvation. Alegre and al. demonstrated[269] that anodes suffered higher degradation rates than cathodes, after fuel starvation, showing 4.6 times the NP size than before the starvation. An aggressive catalyst degradation occurred due to the cell potential reversal.[269] Taniguchi et al.[253] observed that the decrease of

cathodic ECSA in a starved cell is directly related to the mean NP size increase, accompanied with the disappearance of the smallest particles.

These performance degradation mechanisms in a running system occur during (1) a long-term operation, (2) a transient operation, or (3) after an incident usually causing irreversible cell damage and consequent abrupt reduction of the cell lifetime.[253] Various degradation processes, causes, and symptoms are presented in **Table 3**.

The HT-PEMFC durability testing under real operating conditions is time-consuming and expensive, therefore, ASTs are used in evaluating cell degradation mechanisms and ensuring reproducibility of results.[252] These protocols are developed to induce and accelerate material degradation, often targeting specific cell components, and monitoring distinct physical values. The Fuel Cell Commercialization Conference of Japan (FCCJ) suggested measuring the ratio of C corrosion/catalyst degradation via two different protocols. Their goal was to separate (1) start-stop and (2) load-cycle conditions during FC vehicle testing.[236] Depending on the cell material of interest, various ASTs are developed targeting different parameters. Measuring the loss in ECSA, and particle size change, during potential cycling is often used in evaluating durability and degradation.[236,237] The contribution of different degradation mechanisms can be estimated by calculating the theoretical ECSA loss, obtained from the particle size measurements, and comparing it to the experimentally measured ECSA loss.[250] Some of the representative recent work on the ASTs are presented in **Table 4**.

Cleemann et al. studied stabilities of three different carbon support materials, (1) Vulcan CB, (2) GCB, and (3) MWCNTs, under potential cycling conditions.[31] The GCB showed better stability and longer durability in HT-PEMFC. Selvaganesh et al. showed that using GCB as a support for Pt NPs and its alloys improved catalyst stability, compared to non-GCB. Pawlyta et al. recently conducted a study on the relationship between carbon support structure and cell durability by comparing CB with structure-modified C support, induced by high-temperature heat treatment.[264] They deposited Pt NPs on different C supports. Their ADT protocol consisted of ECSA monitoring over the 5000 potential-sweeping cycles (0.6–1.2 V vs RHE, at 0.1 V s^{-1}). The

Table 4. Summary of recent ASTs of HT-PEMFCs.

Catalyst	Conditions	Test results	Highlight	Year	Ref.
1. Pt/NrEGO$_2$-CB$_3$ 2. Pt/C	AST in RDE: 0.6–1.0 V, 2.0 м H$_3$PO$_4$, 30 000 cycles HT-PEM durability: 0.4 A for 100 h, 150 °C, dry H$_2$/O$_2$ AST in a cell: Cycling 0.3A-OCV, 210 cycles	ECSA loss: 1. 13.65% 2. 97.99% Cell degradation: 1. 0.02 mV h^{-1} 2. 1.14 mV h^{-1} Particle size after AST: 1. 5.46 ± 1.46 nm 2. 6.78 ± 1.39 nm	Pt/NrEGO$_2$-CB$_3$ achieved high Pt efficiency and inhibition in R$_c$ and R$_{mt}$.	2022	[236]
1. Pt/C 2. PtNi/WCB 3. PtNi/C 4. Pt/WCB 5. Pt/CB	AST in RDE: 0.6–1.05 versus RHE, 0.1 м HClO$_4$, 100 mV s^{-1}, 10 000 cycles HT-PEM durability: 0.2 A cm^{-2}, 200 h, 160 °C, dry H$_2$/O$_2$, 0 barG	E½ potential drop/SA$^{a)}$ decline/MA$^{b)}$ decline: 1. 30mV/38.3%/38.5% 2. 5 mV/0.85%/1.59% P$_{max}$$^{c)}$ decrease/R$_{ct}$ increase: 2. 3.2%/0.5mΩ	PtNi/WCB MEA P$_{max}$$^{c)}$ = 0.9 W cm^{-2} decreased by 3.2% after durability tests. Superior durability of PtNi/WCB as the cathode catalyst.	2021	[270]
1. PtPBI/MWCNT 2. Pt/MWCNT 3. Pt/C	EC cell: 0.25–1.2 V, 25 °C, 0.1м HClO$_4$, 50 mV s^{-1}	ECSA loss [%]: 1. 21% 2. 34% 3. 78%	The Pt-PBI/MWCNT ECSA loss lower than commercial Pt–C in HT-PEMFC test.	2020	[225]
1. Pt/C 2. Pt/gC$_3$N$_4$-C (nanosheets)	CA: O$_2$-sat., 2.0 м H$_3$PO$_4$, 0.6 V versus RHE, 1 h ADT in RDE: 0.6–1.2 V versus RHE, 25 °C, O$_2$-sat. 2.0 м H$_3$PO$_4$, 100 mV s^{-1}, 5000 cycles HT-PEM durability: 0.2A cm^{-2}, 100 h, 150 °C, dry H$_2$/O$_2$, 0 barG	i retention: 1. 59.5% 2. 79.4% ECSA retention: 1. 54% 2. 87.6% P$_{max}$$^{c)}$ decrease: 1. 23.5% 2. 10.7%	Poor electronic conductivity of Pt/g/C$_3$N$_4$-C compensated by CB.	2020	[237]
1. Pt/GCNT 2. Pt/CNT 3. Pt/C	AST test: 0.25–1.2 V in N$_2$ 0.1м HClO$_4$ at 100mV s^{-1} for 1000 cycles AST Triangle-wave: 0.6 –1.0 V at 50 mV s^{-1} potential cycling for 10 000 cycles	ECSA loss: 1. 37.3% 2. 39.5% 3. 42.3% i retention @0.6V: 1. 61% 2. 67% 3. 60%	P @ 0.6 V, 160 °C: 1. 0.22 W cm^{-2} 2. 0.18 W cm^{-2} 3. 0.12 W cm^{-2}	2020	[227]
1. Pt/MWCNT (30%Pt) 2. Pt/MWCNT (42%Pt) 3. Pt/MWCNT (26%Pt) 4. Pt/MWCNT (29%Pt) 5. Pt/MWCNT (34%Pt) 6. Pt/C (40%Pt)	AST EC cell: 0.6–1.2 V, H$_2$/N$_2$, 0.1 м HClO$_4$, 50 mV s^{-1}, 5000 cycles AST triangle-wave: 0.6–1.0 V, 50 mV s^{-1}, 10 000 cycles HT-PEMFC durability: 0.1 A cm^{-2}, 400 h, 160 °C, 0 barG	ECSA loss//ECSA retention//Degradation rate: 1. 22%//42%//83.5 μV h^{-1} 2. 34% 3. 43% 4. 27% 5. 68% 6. 46%//29%//64.5 [μV h^{-1}]	A facile microwave-assisted Pt/MWCNT catalyst synthesis for HT-PEMFC.	2019	[271]
1. Comm. Pt-CB	AST FCCJ EC cell: 1.0–1.5V versus RHE, 500 mV s^{-1}, 0.5 м H$_2$SO$_4$ AST: 10 000 cycles	ECSA loss//Particle size after AST: 1. 50%//4.9 ± 0.5 nm 2. 40%//5.0 ± 0.7 nm 3. 5%//3.2 ± 0.2 nm	CNT/ABPBI-Pt@IL had 0.51 W cm^{-2} P$_{max}$, higher than commercial Pt-CB, 0.37 W cm^{-2}.	2018	[272]

(Continued)

**ADVANCED
SCIENCE NEWS**
www.advancedsciencenews.com

**ADVANCED
MATERIALS**
www.advmat.de

Table 4. (Continued).

Catalyst	Conditions	Test results	Highlight	Year	Ref.
2. CNT/AB-PBI-Pt					
3. CNT/AB-PBI-Pt@IL					
1. Pt/GO	EC cell:	ECSA loss:	The better HT-PEMFC performance is attributed to the high graphitization properties of the PBI/GNP MEA.	2017	[197]
2. Pt/GNP	-0.25–1.2 V, 20 mV s^{-1}, 25 °C, 0.1 M HClO$_4$, 1000 cycles	1. 19%			
3. Pt/C		2. 16%			
		3. 46%			
1. ox-CNT/Pt	AST FCCJ EC cell:	ECSA loss:	Commercial Pt-CB showed the lowest P_{max} [c] (0.17 W cm^{-2}). The ox-CNT/Pt reached 0.27 and oxCNT/Pt/PBI 0.42 W cm^{-2} P_{max}.	2017	[273]
	1.0–1.5V versus RHE, 500 mV s^{-1}, 0.5 M H$_2$SO$_4$	1. 50% (50 000 cycles)			
		2. 48% (350 000 cycles)			
		3. 50% (10 000 cycles)			
2. ox-CNT/Pt/PBI		Pt NP size increase before/after cycling:			
3. CB/Pt		1. 3.7 ± 0.5 5.8 ± 2.6			
		2. 3.8 ± 0.6 6.0 ± 2.1			
		3. 3.9 ± 0.6 5.0 ± 0.1			
1. MWNT/PyPBI/Pt	AST FCCJ EC cell: 1.0–1.5V versus RHE, 500 mV s^{-1}, 0.1 M HClO$_4$, 25 °C	ECSA retention:	The FC test under 120 °C showed that the mass power density of MWNT/PyPBI/Pt cluster was 6.7 times higher than that of commercial CB/Pt.	2016	[250]
2. CB/Pt		1. ≈50% (200 000 cycles)			
3. CB/PyPBI/Pt		2. 54% (10 000 cycles)			
2. 40Pt/Vulcan$_{lab}$		3. 42% (40 000 cycles)			
3. Pt/Vulcan$_{comm.}$					
1. MWNTs/para-PyPBI/Pt	AST FCCJ EC cell: 1.0–1.5V versus RHE, 500 mV s^{-1}, 0.1 M HClO$_4$, 25 °C	ECSA loss:	MWNTs/para-PyPBI/Pt showed P_{max} [c] 0.41 W cm^{-2}, 2.5 and 2 times more than the CB/Pt and MWNTs/para-PyPBI/Pt, in HT-PEM.	2015	[274]
2. MWNTs/para-PyPBI-PA/Pt		1. 16.3%			
3. CB/Pt		2. 20%			
		3. 47%			

[a] Mass activity; [b] Specific activity; [c] Peak power density.

total ECSA loss was recorded for Pt/CB-1700 after 5000 cycles. The Pt/CB-0 and Pt/CB-3000 samples had less ECSA degradation, retaining 35% and 73% of the initial ECSA, respectively. They also associated C support stability with the degree of graphitization. Despite the limited degree of graphitization, strong interactions between Pt and C support were formed, inhibiting the C corrosion, and increasing the durability of the whole system.

As reported above, the CL degradation is predominantly governing the HT-PEMFC lifetime. Studies have been performed to understand and quantify the corresponding mechanisms and phenomena mainly relating to C support and metallic NPs. Understanding these HT-PEMFC degradation mechanisms is the key for mass commercialization of the technology.

6. Conclusion

The purpose of this discussion is to inspire readers to develop catalysts that can tackle the current challenges of durability in high-temperature fuel cells. As we gain a deeper understanding of how catalyst layers degrade at high temperatures, there is inexhaustible potential for improving electrocatalysts and catalyst supports. Developing catalysts for high-temperature proton exchange membrane fuel cells (HT-PEMFCs) is essential for the long-term viability and commercialization of fuel cell technology. Combining approaches like Pt alloying with transition metals, synthesizing hollow nanoparticles, and anchoring them in carbon-based nanostructures can effectively maximize efficiency and fuel cell durability. Another significant durability issue during high-potential cycles can be addressed by changing or adjusting the carbon support material. Based on our understanding and review of the literature, we propose the following potential research areas for the development of high-temperature catalysts: (1) the development of extremely robust catalytic supports, such as more graphitized carbon materials, that can withstand high temperatures; (2) improving the interaction between supports and catalysts to stabilize Pt-based nanoparticles and improve catalytic activity; and (3) researching novel catalysts to develop exceptionally robust PGM-free catalysts.

Conflict of Interest

The authors declare no conflict of interest.

Keywords

[1] D. Aili, L. N. Cleemann, Q. Li, J. O. Jensen, E. Christensen, N. J. Bjerrum, *J. Mater. Chem.* **2012**, *22*, 5444.

[2] D. Aili, J. Zhang, M. T. Dalsgaard Jakobsen, H. Zhu, T. Yang, J. Liu, M. Forsyth, C. Pan, J. O. Jensen, L. N. Cleemann, S. P. Jiang, Q. Li, *J. Mater. Chem. A* **2016**, *4*, 4019.

[3] E. Aktas, J. Jiménez-López, K. Azizi, T. Torres, E. Palomares, *Nanoscale Horiz.* **2020**, *5*, 1415.

[4] M. Urbani, G. De La Torre, M. K. Nazeeruddin, T. Torres, *Chem. Soc. Rev.* **2019**, *48*, 2738.

[5] L. Zhang, B. Zhang, J. Chen, L. Jin, W. Deng, J. Tang, H. Zhang, H. Pan, M. Zhu, W. Yang, Z. L. Wang, *Adv. Mater.* **2016**, *28*, 1650.

[6] X. Zhao, A. Nashalian, I. W. Ock, S. Popoli, J. Xu, J. Yin, T. Tat, A. Libanori, G. Chen, Y. Zhou, J. Chen, *Adv. Mater.* **2022**, *34*, 2204238.

[7] M. Prokop, P. Capek, M. Vesely, M. Paidar, K. Bouzek, K. B. M. Prokop, M. Vesely, P. Capek, M. Paidar, *Electrochim. Acta* **2022**, *413*, 140121.

[8] B. G. Pollet, S. S. Kocha, I. Staffell, *Curr. Opin. Electrochem.* **2019**, *16*, 90.

[9] D. E. Hussin, Y. Budak, Y. Devrim, *Int. J. Energy Res.* **2022**, *46*, 4174.

[10] A. L. Rangel-Cárdenas, G. J. M. Koper, *Materials* **2017**, *10*, 576.

[11] C. I. T. de Grotthius, *Philos. Mag.* **1806**, *25*, 330.

[12] A. Unnikrishnan, N. Rajalakshmi, V. M. Janardhanan, *Electrochim. Acta* **2019**, *293*, 128.

[13] Y. Wang, D. F. Ruiz Diaz, K. S. Chen, Z. Wang, X. C. Adroher, *Mater. Today* **2020**, *32*, 178.

[14] R. E. Rosli, A. B. Sulong, W. R. W. Daud, M. A. Zulkifley, T. Husaini, M. I. Rosli, E. H. Majlan, M. A. Haque, *Int. J. Hydrogen Energy* **2017**, *42*, 9293.

[15] D. Aili, D. Henkensmeier, S. Martin, B. Singh, Y. Hu, J. O. Jensen, L. N. Cleemann, Q. Li, *Electrochem. Energy Rev.* **2020**, *3*, 793.

[16] T. Søndergaard, L. N. Cleemann, H. Becker, D. Aili, T. Steenberg, H. A. Hjuler, L. Seerup, Q. Li, J. O. Jensen, *J. Power Sources* **2017**, *342*, 570.

[17] D. Aili, J. Yang, K. Jankova, D. Henkensmeier, Q. Li, *J. Mater. Chem. A* **2020**, *8*, 12854.

[18] L. Vilčiauskas, M. E. Tuckerman, G. Bester, S. J. Paddison, K. D. Kreuer, *Nat. Chem.* **2012**, *4*, 461.

[19] S. Authayanun, K. Im-Orb, A. Arpornwichanop, *Chin. J. Catal.* **2015**, *36*, 473.

[20] S. Martin, Q. Li, T. Steenberg, J. O. Jensen, *J. Power Sources* **2014**, *272*, 559.

[21] M. Khorshidian, M. Sedighi, *Iran. J. Hydrog. Fuel Cell* **2019**, *2*, 91.

[22] N. Bevilacqua, M. G. George, A. Bazylak, R. Zeis. *ECS Trans* **2017**, *80*, 409.

[23] K. B. M. Prokop, M. Vesely, P. Capek, M. Paidar, *Electrochim. Acta* **2022**, *413*, 140133.

[24] H. Liang, H. Su, B. G. Pollet, V. Linkov, S. Pasupathi, *J. Power Sources* **2014**, *266*, 107.

[25] H. Liang, H. Su, B. G. Pollet, S. Pasupathi, *J. Power Sources* **2015**, *288*, 121.

[26] H. Su, T. C. Jao, O. Barron, B. G. Pollet, S. Pasupathi, *J. Power Sources* **2014**, *267*, 155.

[27] C. Pan, R. He, Q. Li, J. O. Jensen, N. J. Bjerrum, H. A. Hjulmand, A. B. Jensen, *J. Power Sources* **2005**, *145*, 392.

[28] T. Engl, J. Käse, L. Gubler, T. J. Schmidt, *ECS Electrochem. Lett.* **2014**, *3*, F47.

[29] T. Søndergaard, L. N. Cleemann, H. Becker, T. Steenberg, H. A. Hjuler, L. Seerup, Q. Li, J. O. Jensen, *J. Electrochem. Soc.* **2018**, *165*, F3053.

[30] J. T. Wang, R. F. Savinell, J. Wainright, M. Litt, H. Yu, *Electrochim. Acta* **1996**, *41*, 193.

[31] L. N. Cleemann, F. Buazar, Q. Li, J. O. Jensen, C. Pan, T. Steenberg, S. Dai, N. J. Bjerrum, *Fuel Cells* **2013**, *13*, 822.

[32] C. Song, *Catal. Today* **2002**, *77*, 17.

[33] S. Authayanun, M. Mamlouk, K. Scott, A. Arpornwichanop, *Appl. Energy* **2013**, *109*, 192.

[34] M. Saeeda, F. Nadeem, M. A. Dutt, *IJCBS* **2019**, *16*, 124.

[35] J. Marquis, M. O. Coppens, *Chem. Eng. Sci.* **2013**, *102*, 151.

[36] R. Zeis, *Beilstein J. Nanotechnol.* **2015**, *6*, 68.

[37] Y. Shao, G. Yin, Z. Wang, Y. Gao, *J. Power Sources* **2007**, *167*, 235.

[38] L. van Biert, M. Godjevac, K. Visser, P. V. Aravind, *J. Power Sources* **2016**, *327*, 345.

[39] S. Authayanun, M. Mamlouk, K. Scott, A. Arpornwichanop, *Appl. Energy* **2013**, *109*, 192.

[40] T. R. Garrick, T. E. Moylan, M. K. Carpenter, A. Kongkanand, *J. Electrochem. Soc.* **2016**, *164*, F55.

[41] P. Pei, Y. Meng, D. Chen, P. Ren, M. Wang, X. Wang, *Energy* **2023**, *265*, 126341.

[42] S. J. C. Cleghorn, D. K. Mayfield, D. A. Moore, J. C. Moore, G. Rusch, T. W. Sherman, N. T. Sisofo, U. Beuscher, *J. Power Sources* **2006**, *158*, 446.

[43] R. Abid, D. Version, Dynamic Performance of a PEM Fuel Cell System, Doctoral dissertation, Technical University of Denmark, **2013**.

[44] S. S. Araya, F. Zhou, V. Liso, S. L. Sahlin, J. R. Vang, S. Thomas, X. Gao, C. Jeppesen, S. K. Kær, *Int. J. Hydrogen Energy* **2016**, *41*, 21310.

[45] Y. Shao-Horn, W. C. Sheng, S. Chen, P. J. Ferreira, E. F. Holby, D. Morgan, *Top. Catal.* **2007**, *46*, 285.

[46] F. Valle, Electrocatalyst degradation in high temperature PEM fuel cells, Doctoral dissertation, University of Trieste **2014**.

[47] M. Bodner, H. R. García, T. Steenberg, C. Terkelsen, S. M. Alfaro, G. S. Avcioglu, A. Vassiliev, S. Primdahl, H. A. Hjuler, *Int. J. Hydrogen Energy* **2019**, *44*, 12793.

[48] L. Mølmen, K. Eiler, L. Fast, P. Leisner, E. Pellicer, *APL Mater.* **2021**, *9*, 040702.

[49] Z. Duan, G. Wang, *J. Phys. Chem. C* **2013**, *117*, 6284.

[50] J. C. Dong, X. G. Zhang, V. Briega-Martos, X. Jin, J. Yang, S. Chen, Z. L. Yang, D. Y. Wu, J. M. Feliu, C. T. Williams, Z. Q. Tian, J. F. Li, *Nature Energy* **2018**, *4*, 60.

[51] N. Hoshi, K. Saikawa, M. Nakamura, *Electrochem. Commun.* **2019**, *106*, 106536.

[52] Q. He, X. Yang, W. Chen, S. Mukerjee, B. Koel, S. Chen, *Phys. Chem. Chem. Phys.* **2010**, *12*, 12544.

[53] C. M. Sánchez-Sánchez, J. Solla-Gullón, F. J. Vidal-Iglesias, A. Aldaz, V. Montiel, E. Herrero, *J. Am. Chem. Soc.* **2010**, *132*, 5622.

[54] H. Cheng, Z. Cao, Z. Chen, M. Zhao, M. Xie, Z. Lyu, Z. Zhu, M. Chi, Y. Xia, *Nano Lett.* **2019**, *19*, 4997.

[55] B. Y. Xia, H. Bin Wu, Y. Yan, X. W. Lou, X. Wang, *J. Am. Chem. Soc.* **2013**, *135*, 9480.

[56] B. Y. Xia, H. Bin Wu, X. Wang, X. W. Lou, *Angew. Chem. Int., Ed. Engl.* **2013**, *52*, 12337.

[57] L. Huang, S. Zaman, X. Tian, Z. Wang, W. Fang, B. Y. Xia, *Acc. Chem. Res.* **2021**, *54*, 311.

[58] L. Wang, M. Imura, Y. Yamauchi, *ACS Appl. Mater. Interfaces* **2012**, *4*, 2865.

[59] B. Y. Xia, W. T. Ng, H. Bin Wu, X. Wang, X. W. Lou, *Angew. Chem., Int. Ed.* **2012**, *51*, 7213.

[60] N. Bevilacqua, T. Asset, M. A. Schmid, H. Markötter, I. Manke, P. Atanassov, R. Zeis, *J Power Sources* **2021**, *7*, 100042.

[61] Z. Peng, H. Yang, *Nano Today* **2009**, *4*, 143.

[62] M. Wu, C. Chen, Y. Zhao, E. Zhu, Y. Li, *Front. Chem.* **2021**, *9*, 443.

[63] L. Ma, C. Wang, B. Y. Xia, K. Mao, J. He, X. Wu, Y. Xiong, X. W. Lou, *Angew. Chem. Int. Ed., Engl.* **2015**, *54*, 5666.

[64] A. Abdelhafiz, B. Zhao, Z. Xiao, J. Zeng, X. Deng, J. Lang, Y. Ding, H. Song, M. Liu, *ACS Appl. Mater. Interfaces* **2020**, *12*, 49510.

[65] Y. Jang, K. H. Choi, D. Y. Chung, J. E. Lee, N. Jung, Y. E. Sung, *ChemSusChem* **2017**, *10*, 3063.

[66] P. Schneider, M. Batool, A. O. Godoy, R. Singh, D. Gerteisen, J. Jankovic, N. Zamel, *J. Electrochem. Soc.* **2023**, *170*, 024506.

[67] M. Rau, A. Niedergesäß, C. Cremers, S. Alfaro, T. Steenberg, H. A. Hjuler, *Fuel Cells* **2016**, *16*, 577.

[68] M. Bodner, J. J. Bentzen, V. A. Dahl, S. M. Alfaro, T. Steenberg, H. A. Hjuler, S. B. Simonsen, *J. Electrochem. Soc.* **2019**, *166*, F1105.

[69] M. Rück, A. Bandarenka, F. Calle-Vallejo, A. Gagliardi, *J. Phys. Chem. Lett.* **2018**, *9*, 4463.

[70] F. J. Perez-Alonso, D. N. McCarthy, A. Nierhoff, P. Hernandez-Fernandez, C. Strebel, I. E. L. Stephens, J. H. Nielsen, I. Chorkendorff, *Angew. Chem. Int. Ed., Engl.* **2012**, *51*, 4641.

[71] S. Y. Lim, S. Martin, G. Gao, Y. Dou, S. B. Simonsen, J. O. Jensen, Q. Li, K. Norrman, S. Jing, W. Zhang, *Adv. Funct. Mater.* **2021**, *31*, 2006771.

[72] H. Tang, K. Geng, D. Aili, Q. Ju, J. Pan, G. Chao, X. Yin, X. Guo, Q. Li, N. Li, *Nat. Commun.* **2022**, *13*, 1.

[73] L. Huang, M. Wei, R. Qi, C. L. Dong, D. Dang, C. C. Yang, C. Xia, C. Chen, S. Zaman, F. M. Li, B. You, B. Y. Xia, *Nat. Commun.* **2022**, *13*, 1.

[74] B. Y. Xia, Y. Yan, N. Li, H. Bin Wu, X. W. D. Lou, X. Wang, *Nat. Energy* **2016**, *1*, 1.

[75] H. Wang, R. Wang, S. Sui, T. Sun, Y. Yan, S. Du, *Automot. Innov.* **2021**, *4*, 144.

[76] U. A. Paulus, A. Wokaun, G. G. Scherer, T. J. Schmidt, V. Stamenkovic, N. M. Markovic, P. N. Ross, *Electrochim. Acta* **2002**, *47*, 3787.

[77] E. Antolini, J. R. C. Salgado, E. R. Gonzalez, *J. Power Sources* **2006**, *160*, 957.

[78] C. V. Rao, J. Parrondo, S. L. Ghatty, B. Rambabu, *J. Power Sources* **2010**, *195*, 3425.

[79] N. Shroti, M. K. Daletou, *Int. J. Hydrogen Energy* **2022**, *47*, 16235.

[80] P. Stonehart, *Stonehart. Ber. Bunsenges. Phys. Chem.* **1990**, *94*, 913.

[81] D. Aili, D. Henkensmeier, S. Martin, B. Singh, Y. Hu, J. O. Jensen, L. N. Cleemann, Q. Li, *Electrochem. Energy Rev.* **2020**, *3*, 793.

[82] I. E. L. Stephens, A. S. Bondarenko, U. Grønbjerg, J. Rossmeisl, I. Chorkendorff, *Energy Environ. Sci.* **2012**, *5*, 6744.

[83] J. Greeley, I. E. L. Stephens, A. S. Bondarenko, T. P. Johansson, H. A. Hansen, T. F. Jaramillo, J. Rossmeisl, I. Chorkendorff, J. K. Nørskov, *Nat. Chem.* **2009**, *1*, 552.

[84] M. Mamlouk, K. Scott, *J. Power Sources* **2011**, *196*, 1084.

[85] J. E. Lim, U. J. Lee, S. H. Ahn, E. A. Cho, H. J. Kim, J. H. Jang, H. Son, S. K. Kim, *Appl. Catal. B* **2015**, *165*, 495.

[86] K. S. Lee, S. J. Yoo, D. Ahn, S. K. Kim, S. J. Hwang, Y. E. Sung, H. J. Kim, E. Cho, D. Henkensmeier, T. H. Lim, J. H. Jang, *Electrochim. Acta* **2011**, *56*, 8802.

[87] A. Kulkarni, S. Siahrostami, A. Patel, J. K. Nørskov, *Chem. Rev.* **2018**, *118*, 2302.

[88] T. Kaito, H. Tanaka, H. Mitsumoto, S. Sugawara, K. Shinohara, H. Ariga, H. Uehara, S. Takakusagi, K. Asakura, *J. Phys. Chem. C* **2016**, *120*, 11519.

[89] Y. Li, L. Jiang, S. Wang, G. Sun, *Chin. J. Catal.* **2016**, *37*, 1134.

[90] Q. Zhang, R. Yue, F. Jiang, H. Wang, C. Zhai, P. Yang, Y. Du, *Gold Bull.* **2013**, *46*, 175.

[91] Y. H. Chung, S. J. Kim, D. Y. Chung, H. Y. Park, Y. E. Sung, S. J. Yoo, J. H. Jang, *Chem. Commun.* **2015**, *51*, 2968.

[92] Z. Jusys, T. J. Schmidt, L. Dubau, K. Lasch, L. Jörissen, J. Garche, R. J. Behm, *J. Power Sources* **2002**, *105*, 297.

[93] H. Liu, C. Li, D. Chen, P. Cui, F. Ye, J. Yang, *Sci. Rep.* **2017**, *7*, 1.

[94] C. Wang, J. S. Spendelow, *Curr. Opin. Electrochem.* **2021**, 100715.

[95] F. Wang, Q. Zhang, Z. Rui, J. Li, J. Liu, *ACS Appl. Mater. Interfaces* **2020**, *12*, 30381.

[96] E. B. Tetteh, C. Gyan-Barimah, H. Y. Lee, T. H. Kang, S. Kang, S. Ringe, J. S. Yu, *ACS Appl. Mater. Interfaces* **2022**, *14*, 25246.

[97] F. de J. Anaya-Castro, M. Beltrán-Gastélum, O. Morales Soto, S. Pérez-Sicairos, S. W. Lin, B. Trujillo-Navarrete, F. Paraguay-Delgado, L. J. Salazar-Gastélum, T. Romero-Castañón, E. Reynoso-Soto, R. M. Félix-Navarro, M. I. Salazar-Gastélum, *Nanomaterials* **2021**, *11*, 3156.

[98] J. Durst, M. Lopez-Haro, L. Dubau, M. Chatenet, Y. Soldo-Olivier, L. Guétaz, P. Bayle-Guillemaud, F. Maillard, *J. Phys. Chem. Lett.* **2014**, *5*, 434.

[99] J. Wang, G. Wu, W. Wang, W. Xuan, J. Jiang, J. Wang, L. Li, W. F. Lin, W. Ding, Z. Wei, *J. Mater. Chem. A* **2019**, *7*, 19786.

[100] W. Zhao, Y. Ye, W. Jiang, J. Li, H. Tang, J. Hu, L. Du, Z. Cui, S. Liao, *J. Mater. Chem. A* **2020**, *8*, 15822.

[101] T. Suzuki, *ECS Trans.* **2016**, *75*, 423.

[102] D. D. Papadias, R. K. Ahluwalia, N. Kariuki, D. Myers, K. L. More, D. A. Cullen, B. T. Sneed, K. C. Neyerlin, R. Mukundan, R. L. Borup, *J. Electrochem. Soc.* **2018**, *165*, F3166.

[103] W. Lei, M. Li, L. He, X. Meng, Z. Mu, Y. Yu, F. M. Ross, W. Yang, *Nano Res.* **2020**, *13*, 638.

[104] Z. Wang, X. Yao, Y. Kang, L. Miao, D. Xia, L. Gan, *Adv. Funct. Mater.* **2019**, *29*, 1902987.

[105] Q. He, B. Shyam, M. Nishijima, D. Ramaker, S. Mukerjee, *J. Phys. Chem. C* **2013**, *117*, 4877.

[106] M. Mamlouk, J. H. Jang, K. Scott, *J. Fuel Cell Sci. Technol.* **2012**, *9*, 11002.

[107] N. Becknell, Y. Kang, C. Chen, J. Resasco, N. Kornienko, J. Guo, N. M. Markovic, G. A. Somorjai, V. R. Stamenkovic, P. Yang, *J. Am. Chem. Soc.* **2015**, *137*, 15817.

[108] W. Gong, Z. Jiang, R. Wu, Y. Liu, L. Huang, N. Hu, P. Tsiakaras, P. K. Shen, *Appl. Catal. B* **2019**, *246*, 277.

[109] V. R. Stamenkovic, B. Fowler, B. S. Mun, G. Wang, P. N. Ross, C. A. Lucas, N. M. Markovic, *Science* **2007**, *315*, 493.

[110] C. Chen, Y. Kang, Z. Huo, Z. Zhu, W. Huang, H. L. Xin, J. D. Snyder, D. Li, J. A. Herron, M. Mavrikakis, M. Chi, K. L. More, Y. Li, N. M. Markovic, G. A. Somorjai, P. Yang, V. R. Stamenkovic, *Science* **2014**, *343*, 1339.

[111] M. Li, Z. Zhao, T. Cheng, A. Fortunelli, C. Y. Chen, R. Yu, Q. Zhang, L. Gu, B. V. Merinov, Z. Lin, E. Zhu, T. Yu, Q. Jia, J. Guo, L. Zhang, W. A. Goddard, Y. Huang, X. Duan, *Science* **2016**, *354*, 1414.

[112] B. Han, C. E. Carlton, A. Kongkanand, R. S. Kukreja, B. R. Theobald, L. Gan, R. O'Malley, P. Strasser, F. T. Wagner, Y. Shao-Horn, *Energy Environ. Sci.* **2015**, *8*, 258.

[113] J. Wang, X. Zhou, B. Li, D. Yang, H. Lv, Q. Xiao, P. Ming, X. Wei, C. Zhang, *Int. J. Hydrogen Energy* **2020**, *45*, 8930.

**ADVANCED
SCIENCE NEWS**

www.advancedsciencenews.com

**ADVANCED
MATERIALS**

www.advmat.de

[114] C. Y. Ahn, S. Kim, H. J. Choi, J. Lee, S. Y. Kang, O. H. Kim, H. Shim, Y. S. Kim, Y. E. Sung, O. J. Kwon, Y. H. Cho, *Int. J. Hydrogen Energy* **2022**, *47*, 1863.

[115] J. Wang, B. Li, D. Yang, H. Lv, C. Zhang, *RSC Adv.* **2018**, *8*, 18381.

[116] F. Dionigi, C. C. Weber, M. Primbs, M. Gocyla, A. M. Bonastre, C. Spöri, H. Schmies, E. Hornberger, S. Kühl, J. Drnec, M. Heggen, J. Sharman, R. E. Dunin-Borkowski, P. Strasser, *Nano Lett.* **2019**, *19*, 6876.

[117] J. Choi, Y. J. Lee, D. Park, H. Jeong, S. Shin, H. Yun, J. Lim, J. Han, E. J. Kim, S. S. Jeon, Y. Jung, H. Lee, B. J. Kim, *Energy Environ. Sci.* **2020**, *13*, 4921.

[118] Z. Yang, L. Shang, X. Xiong, R. Shi, G. I. N. Waterhouse, T. Zhang, *Chemistry* **2020**, *26*, 4090.

[119] Z. Meng, F. Xiao, Z. Wei, X. Guo, Y. Zhu, Y. Liu, G. Li, Z. Q. Yu, M. Shao, W. Y. Wong, *Nano Res.* **2019**, *12*, 2954.

[120] M. Gong, J. Zhu, M. Liu, P. Liu, Z. Deng, T. Shen, T. Zhao, R. Lin, Y. Lu, S. Yang, Z. Liang, S. M. Bak, E. Stavitski, Q. Wu, R. R. Adzic, H. L. Xin, D. Wang, *Nanoscale* **2019**, *11*, 20301.

[121] Y. H. Chung, D. Y. Chung, N. Jung, H. Y. Park, Y. E. Sung, S. J. Yoo, *Int. J. Hydrogen Energy* **2014**, *39*, 14751.

[122] F. Xiao, Q. Wang, G. L. Xu, X. Qin, I. Hwang, C. J. Sun, M. Liu, W. Hua, H. wen Wu, S. Zhu, J. C. Li, J. G. Wang, Y. Zhu, D. Wu, Z. Wei, M. Gu, K. Amine, M. Shao, *Nat. Catal.* **2022**, *5*, 503.

[123] Y. Hu, T. Shen, X. Zhao, J. Zhang, Y. Lu, J. Shen, S. Lu, Z. Tu, H. L. Xin, D. Wang, *Appl. Catal. B* **2020**, *279*, 119370.

[124] H. Yano, M. Kataoka, H. Yamashita, H. Uchida, M. Watanabe, *Langmuir* **2007**, *23*, 6438.

[125] M. Sakthivel, I. Radev, V. Peinecke, J.-F. Drillet, *J. Electrochem. Soc.* **2015**, *162*, F901.

[126] M. G. H. Al-Tememy, Y. Devrim, *Int. J. Energy Res.* **2021**, *45*, 3343.

[127] X. Deng, S. Yin, S. Wu, M. Sun, Z. Li, Z. Xie, Y. Liang, Q. Huang, *Int. J. Hydrogen Energy* **2019**, *44*, 2752.

[128] F. Chang, Z. Bai, M. Li, M. Ren, T. Liu, L. Yang, C. J. Zhong, J. Lu, *ACS Appl. Mater. Interfaces* **2020**, *20*, 2416.

[129] M. S. M. Yusof, A. A. Jalil, A. Ahmad, S. Triwahyono, M. H. D. Othman, T. A. T. Abdullah, M. L. Firmansyah, H. D. Setiabudi, A. Johari, W. Nabgan, *Int. J. Hydrogen Energy* **2019**, *44*, 20760.

[130] K. Sasaki, K. A. Kuttiyiel, R. R. Adzic, *Curr. Opin. Electrochem.* **2020**, *21*, 368.

[131] A. Brouzgou, A. Seretis, S. Song, P. K. Shen, P. Tsiakaras, *Int. J. Hydrogen Energy* **2021**, *46*, 13865.

[132] M. Wesselmark, B. Wickman, C. Lagergren, G. Lindbergh, *Electrochim. Acta* **2013**, *111*, 152.

[133] M. Bekmezci, D. B. Subasi, R. Bayat, M. Akin, Z. K. Coguplugil, F. Sen, *New J. Chem.* **2022**, *46*, 21591.

[134] C. Molochas, P. Tsiakaras, *Catalysts* **2021**, *11*, 1127.

[135] K. Hengge, T. Gänsler, E. Pizzutilo, C. Heinzl, M. Beetz, K. J. J. Mayrhofer, C. Scheu, *Int. J. Hydrogen Energy* **2017**, *42*, 25359.

[136] C. Molochas, P. Tsiakaras, *Catalysts* **2021**, *11*, 1127.

[137] G. U. Alpaydin, Y. Devrim, C. O. Colpan, *Int. J. Energy Res.* **2019**, *43*, 3578.

[138] N. Seselj, C. Engelbrekt, Y. Ding, H. A. Hjuler, J. Ulstrup, J. Zhang, *Adv. Energy Mater.* **2018**, *8*, 1702609.

[139] J. Zhang, K. Sasaki, E. Sutter, R. R. Adzic, *Science* **2007**, *315*, 220.

[140] H. Chen, R. Wu, P. K. Shen, *ACS Sustain. Chem. Eng.* **2020**, *8*, 1520.

[141] F. Kong, S. Liu, J. Li, L. Du, M. N. Banis, L. Zhang, G. Chen, K. Doyle-Davis, J. Liang, S. Wang, F. Zhao, R. Li, C. Du, G. Yin, Z. Zhao, X. Sun, *Nano Energy* **2019**, *64*, 103890.

[142] H. Nan, Y. Q. Su, C. Tang, R. Cao, D. Li, J. Yu, Q. Liu, Y. Deng, X. Tian, *Sci. Bull.* **2020**, *65*, 1396.

[143] W. Tu, K. Chen, L. Zhu, H. Zai, E. Bin, X. Ke, C. Chen, M. Sui, Q. Chen, Y. Li, *Adv. Funct. Mater.* **2019**, *29*, 1807070.

[144] R. Lin, L. Che, D. Shen, X. Cai, *Electrochim. Acta* **2020**, *330*, 135251.

[145] W. Tu, W. Luo, C. Chen, K. Chen, E. Zhu, Z. Zhao, Z. Wang, T. Hu, H. Zai, X. Ke, M. Sui, P. Chen, Q. Zhang, Q. Chen, Y. Li, Y. Huang, *Adv. Funct. Mater.* **2020**, *30*, 1908230.

[146] P. Strasser, Q. Fan, M. Devenney, W. H. Weinberg, P. Liu, J. K. Nørskov, *J. Phys. Chem. B* **2003**, *107*, 11013.

[147] N. Tsiouvaras, M. V. Martínez-Huerta, O. Paschos, U. Stimming, J. L. G. Fierro, M. A. Peña, *Int. J. Hydrogen Energy* **2010**, *35*, 11478.

[148] H. Park, D. K. Kim, H. Kim, S. Oh, W. S. Jung, S. K. Kim, *Appl. Surf. Sci.* **2020**, *510*, 145444.

[149] P. Brault, C. Coutanceau, P. C. Jennings, T. Vegge, J. Berndt, A. Caillard, S. Baranton, S. Lankiang, *Int. J. Hydrogen Energy* **2016**, *41*, 22589.

[150] J. Zhu, A. O. Elnabawy, Z. Lyu, M. Xie, E. A. Murray, Z. Chen, W. Jin, M. Mavrikakis, Y. Xia, *Mater. Today* **2020**, *35*, 69.

[151] M. Watanabe, H. Zhu, H. Uchida, *J. Phys. Chem. B* **2000**, *104*, 1762.

[152] D. Zhang, R. Ding, Y. Tang, Y. He, *Langmuir* **2023**, *4*, 1640.

[153] Q. Wang, S. Chen, P. Li, S. Ibraheem, J. Li, J. Deng, Z. Wei, *Appl. Catal. B* **2019**, *252*, 120.

[154] O. V. Tripachev, A. D. Modestov, O. V. Korchagin, V. A. Bogdanovskaya, V. A. Vasilenko, M. V. Radina, *Russ. J. Appl. Chem.* **2020**, *93*, 1743.

[155] M. Semasko, L. Tamasauskaite-Tamasiunaite, V. Kepeniene, A. Balciunaite, J. Vaiciuniene, A. Drabavicius, E. Norkus, *ECS Trans.* **2015**, *68*, 55.

[156] Y. Liang, H. Zhang, Z. Tian, X. Zhu, X. Wang, B. Yi, *J. Phys. Chem. B* **2006**, *110*, 7828.

[157] C. V. S. Almeida, N. A. Galiote, K. I. B. Eguiluz, G. R. Salazar-Banda, V. Del Colle, G. Tremiliosi-Filho, *Electrochim. Acta* **2020**, *351*, 136223.

[158] S. H. Han, H. M. Liu, P. Chen, J. X. Jiang, Y. Chen, *Adv. Energy Mater.* **2018**, *8*, 1801326.

[159] A. A. Vedyagin, Y. V. Shubin, R. M. Kenzhin, P. E. Plyusnin, V. O. Stoyanovskii, *Processes* **2020**, *8*, 928.

[160] L. Huang, M. Wei, N. Hu, P. Tsiakaras, P. Kang Shen, *Appl. Catal. B* **2019**, *258*, 117974.

[161] C. Li, Y. Xu, K. Deng, S. Yin, Z. Wang, H. Xue, X. Li, L. Wang, H. Wang, *J. Mater. Chem. A* **2019**, *7*, 3910.

[162] J. H. Kim, S. Y. Kwon, D. Bhattacharjya, G. S. Chai, J. S. Yu, *J. Catal.* **2013**, *306*, 133.

[163] M. Rethinasabapathy, S. M. Kang, Y. Haldorai, N. Jonna, M. Jankiraman, G. W. Lee, S. C. Jang, B. Natesan, C. Roh, Y. S. Huh, *J. Ind. Eng. Chem.* **2019**, *69*, 285.

[164] Z. Wang, X. Yao, Y. Kang, D. Xia, L. Gan, *Catalysts* **2019**, *9*, 569.

[165] Y. Hu, J. O. Jensen, W. Zhang, L. N. Cleemann, W. Xing, N. J. Bjerrum, Q. Li, *Angew. Chem., Int. Ed.* **2014**, *53*, 3675.

[166] J. Barrio, A. Pedersen, J. Feng, S. C. Sarma, M. Wang, A. Y. Li, H. Yadegari, H. Luo, M. P. Ryan, M. M. Titirici, I. E. L. Stephens, *J. Mater. Chem. A* **2022**, *10*, 6023.

[167] U. Martinez, E. F. Holby, S. K. Babu, K. Artyushkova, L. Lin, S. Choudhury, G. M. Purdy, P. Zelenay, *J. Electrochem. Soc.* **2019**, *166*, F3136.

[168] F. Luo, A. Roy, L. Silvioli, D. A. Cullen, A. Zitolo, M. T. Sougrati, I. C. Oguz, T. Mineva, D. Teschner, S. Wagner, J. Wen, F. Dionigi, U. I. Kramm, J. Rossmeisl, F. Jaouen, P. Strasser, *Nat. Mater.* **2020**, *19*, 1215.

[169] A. Zitolo, V. Goellner, V. Armel, M. T. Sougrati, T. Mineva, L. Stievano, E. Fonda, F. Jaouen, *Nat. Mater.* **2015**, *14*, 937.

[170] D. M. D'Alessandro, *Chem. Commun.* **2016**, *52*, 8957.

[171] A. Pedersen, J. Barrio, A. Li, R. Jervis, D. J. L. Brett, M. M. Titirici, I. E. L. Stephens, *Adv. Energy Mater.* **2022**, *12*, 2102715.

[172] D. Deng, L. Yu, X. Chen, G. Wang, L. Jin, X. Pan, J. Deng, G. Sun, X. Bao, *Angew. Chem., Int. Ed.* **2013**, *52*, 371.

[173] M. Ferrandon, A. J. Kropf, D. J. Myers, K. Artyushkova, U. Kramm, P. Bogdanoff, G. Wu, C. M. Johnston, P. Zelenay, *J. Phys. Chem. C* **2012**, *116*, 16001.

2302207 (24 of 28)

[174] U. Tylus, Q. Jia, K. Strickland, N. Ramaswamy, A. Serov, P. Atanassov, S. Mukerjee, *J. Phys. Chem. C* **2014**, *118*, 8999.

[175] X. Wan, X. Liu, J. Shui, *Prog. Natl. Sci.: Mater. Int.* **2020**, *30*, 721.

[176] D. Xia, X. Tang, S. Dai, R. Ge, A. Rykov, J. Wang, T. H. Huang, K. W. Wang, Y. Wei, K. Zhang, J. Li, L. Gan, F. Kang, *Adv. Mater.* **2023**, *35*, 2204474.

[177] Y. Shao, J. P. Dodelet, G. Wu, P. Zelenay, *Adv. Mater.* **2019**, *31*, 1807615.

[178] L. Yang, J. Shui, L. Du, Y. Shao, J. Liu, L. Dai, Z. Hu, *Adv. Mater.* **2019**, *31*, 1804799.

[179] Y. Hu, J. O. Jensen, C. Pan, L. N. Cleemann, I. Shypunov, Q. Li, *Appl. Catal. B* **2018**, *234*, 357.

[180] Y. Cheng, S. He, S. Lu, J. P. Veder, B. Johannessen, L. Thomsen, M. Saunders, T. Becker, R. De Marco, Q. Li, S. ze Yang, S. P. Jiang, *Adv. Sci.* **2019**, *6*, 1802066.

[181] Y. Cheng, M. Wang, S. Lu, C. Tang, X. Wu, J. P. Veder, B. Johannessen, L. Thomsen, J. Zhang, S. ze Yang, S. Wang, S. P. Jiang, *Appl. Catal. B* **2021**, *284*, 119717.

[182] X. Jin, Y. Li, H. Sun, X. Gao, J. Li, Z. Lü, W. Liu, X. Sun, *Nano Res.* **2022**, 15.

[183] A. Byeon, K. J. Lee, M. J. Lee, J. S. Lee, I. H. Lee, H. Y. Park, S. Y. Lee, S. J. Yoo, J. H. Jang, H. J. Kim, J. Y. Kim, *ChemElectroChem* **2018**, *5*, 1805.

[184] Q. Meyer, C. Yang, Y. Cheng, C. Zhao, *Electrochem. Energy Rev.* **2023**, *6*, 16.

[185] Q. Meyer, C. Yang, Y. Cheng, C. Zhao, *Electrochem. Energy Rev.* **2023**, *6*, 1.

[186] Y. Li, P. Zhang, L. Wan, Y. Zheng, X. Qu, H. Zhang, Y. Wang, K. Zaghib, J. Yuan, S. Sun, Y. Wang, Z. Zhou, S. Sun, *Adv. Funct. Mater.* **2021**, *31*, 2009645.

[187] Z. Chen, J. P. Dodelet, J. Zhang, *Non-Noble Met. Fuel Cell Catal.* **2014**, *9783527333240*, 1.

[188] H. A. Gasteiger, S. S. Kocha, B. Sompalli, F. T. Wagner, *Appl. Catal. B* **2005**, *56*, 9.

[189] R. Gokhale, T. Asset, G. Qian, A. Serov, K. Artyushkova, B. C. Benicewicz, P. Atanassov, *Electrochem. Commun.* **2018**, *93*, 91.

[190] M. J. Workman, A. Serov, L. K. Tsui, P. Atanassov, K. Artyushkova, *ACS Energy Lett.* **2017**, *2*, 1489.

[191] A. Serov, K. Artyushkova, P. Atanassov, *Adv. Energy Mater.* **2014**, *4*, 1301735.

[192] J. Müller-Hülstede, T. Zierdt, H. Schmies, D. Schonvogel, Q. Meyer, C. Zhao, P. Wagner, M. Wark, *J. Power Sources* **2022**, *537*, 231529.

[193] M. A. Abdelkareem, T. Wilberforce, K. Elsaid, E. T. Sayed, E. A. M. Abdelghani, A. G. Olabi, *Int. J. Hydrogen Energy* **2021**, *46*, 23529.

[194] P. K. Mohanta, F. Regnet, L. Jörissen, *Materials* **2018**, *11*, 907.

[195] S. A. Grigoriev, V. N. Fateev, A. S. Pushkarev, I. V. Pushkareva, N. A. Ivanova, V. N. Kalinichenko, M. Y. Presnyakov, X. Wei, *Materials* **2018**, *11*, 1405.

[196] L. Du, Y. Shao, J. Sun, G. Yin, J. Liu, Y. Wang, *Nano Energy* **2016**, *29*, 314.

[197] Y. Devrim, E. D. Arıca, A. Albostan, *Int. J. Hydrogen Energy* **2018**, *43*, 11820.

[198] C. W. B. Bezerra, L. Zhang, H. Liu, K. Lee, A. L. B. Marques, E. P. Marques, H. Wang, J. Zhang, *J. Power Sources* **2007**, *173*, 891.

[199] Y. Chen, K. Azizi, W. Zhang, D. Aili, S. Primdahl, L. N. Cleemann, H. A. Hjuler, Q. Li, *Int. J. Hydrogen Energy* **2022**, *47*, 28615.

[200] M. Uchida, Y. Aoyama, N. Tanabe, N. Yanagihara, N. Eda, A. Ohta, *J. Electrochem. Soc.* **1995**, *142*, 2572.

[201] E. Antolini, R. R. Passos, E. A. Ticianelli, *J. Power Sources* **2002**, *109*, 477.

[202] X. Guo, H. Zhang, *Energy* **2020**, *193*, 116720.

[203] B. C. Cha, S. Jun, B. Jeong, M. Ezazi, G. Kwon, D. Kim, D. H. Lee, *J. Power Sources* **2018**, *401*, 296.

[204] G. de la Torre, G. Bottari, T. Torres, *Adv. Energy Mater.* **2017**, *7*, 1601700.

[205] S. G. Peera, R. Koutavarapu, S. Akula, A. Asokan, P. Moni, M. Selvaraj, J. Balamurugan, S. O. Kim, C. Liu, A. K. Sahu, *Energy Fuels* **2021**, *35*, 11761.

[206] J. Wang, W. Zhu, X. He, S. Yang, *Catal. Commun.* **2008**, *9*, 2163.

[207] C. W. Mason, A. M. Kannan, *ISRN Nanotechnol.* **2011**, *2011*, 1.

[208] M. Endo, Y. A. Kim, T. Hayashi, T. Yanagisawa, H. Muramatsu, M. Ezaka, H. Terrones, M. Terrones, M. S. Dresselhaus, *Carbon* **2003**, *41*, 1941.

[209] S. V. Selvaganesh, P. Sridhar, S. Pitchumani, A. K. Shukla, *J. Electrochem. Soc.* **2013**, *160*, F49.

[210] D. R. Kauffman, A. Star, *Analyst* **2010**, *135*, 2790.

[211] Z. Liu, L. M. Gan, L. Hong, W. Chen, J. Y. Lee, *J. Power Sources* **2005**, *139*, 73.

[212] G. G. Wildgoose, C. E. Banks, R. G. Compton, *Small* **2006**, *2*, 182.

[213] K. Lee, J. Zhang, H. Wang, D. P. Wilkinson, *J. Appl. Electrochem.* **2006**, *36*, 507.

[214] T. Matsumoto, T. Komatsu, K. Arai, T. Yamazaki, M. Kijima, H. Shimizu, Y. Takasawa, J. Nakamura, *Chem. Commun.* **2004**, *4*, 840.

[215] G. Girishkumar, M. Rettker, R. Underhile, D. Binz, K. Vinodgopal, P. McGinn, P. Kamat, *Langmuir* **2005**, *21*, 8487.

[216] R. H. Baughman, A. A. Zakhidov, W. A. De Heer, *Science* **2002**, *297*, 787.

[217] C. Kim, Y. J. Kim, Y. A. Kim, T. Yanagisawa, K. C. Park, M. Endo, M. S. Dresselhaus, *J. Appl. Phys.* **2004**, *96*, 5903.

[218] H. Chu, Y. Shen, L. Lin, X. Qin, G. Feng, Z. Lin, J. Wang, H. Liu, Y. Li, *Adv. Funct. Mater.* **2010**, *20*, 3747.

[219] M. Okamoto, T. Fujigaya, N. Nakashima, *Small* **2009**, *5*, 735.

[220] A. Orfanidi, M. K. Daletou, S. G. Neophytides, *Electrochim. Acta* **2017**, *233*, 218.

[221] T. Fujigaya, M. Okamoto, N. Nakashima, *Carbon* **2009**, *47*, 3227.

[222] M. R. Berber, I. H. Hafez, T. Fujigaya, N. Nakashima, *J. Mater. Chem. A* **2014**, *2*, 19053.

[223] D. Kaewsai, H. L. Lin, T. L. Yu, *Fuel Cells* **2015**, *15*, 361.

[224] D. Kaewsai, H. L. Lin, Y. C. Liu, T. Leon Yu, *Int. J. Hydrogen Energy* **2016**, *41*, 10430.

[225] E. O. Eren, N. Özkan, Y. Devrim, *Int. J. Hydrogen Energy* **2021**, *46*, 29556.

[226] Y. C. Zou, M. Nie, Y. M. Huang, J. Q. Wang, H. L. Liu, *Int. J. Hydrogen Energy* **2011**, *36*, 12343.

[227] Y. Devrim, E. D. Arıca, *Int. J. Hydrogen Energy* **2020**, *45*, 3609.

[228] A. Orfanidi, P. Madkikar, H. A. El-Sayed, G. S. Harzer, T. Kratky, H. A. Gasteiger, *J. Electrochem. Soc.* **2017**, *164*, F418.

[229] N. Pimperl, N. Bevilacqua, M. A. Schmid, P. A. Loichet Torres, H. A. El-Sayed, R. Zeis, K. P. Zeyer, *J. Power Sources* **2021**, *507*, 229971.

[230] D. A. C. Brownson, C. E. Banks, *Analyst* **2010**, *135*, 2768.

[231] M. Liu, R. Zhang, W. Chen, *Chem. Rev.* **2014**, *114*, 5117.

[232] J. Chen, J. J. Bailey, L. Britnell, M. Perez-Page, M. Sahoo, Z. Zhang, A. Strudwick, J. Hack, Z. Guo, Z. Ji, P. Martin, D. J. L. Brett, P. R. Shearing, S. M. Holmes, *Nano Energy* **2022**, *93*, 106829.

[233] A. Marinkas, F. Arena, J. Mitzel, G. M. Prinz, A. Heinzel, V. Peinecke, H. Natter, *Carbon* **2013**, *58*, 139.

[234] H. Wang, T. Maiyalagan, X. Wang, *ACS Catal.* **2012**, *2*, 781.

[235] Z. Ji, M. Perez-Page, J. Chen, R. G. Rodriguez, R. Cai, S. J. Haigh, S. M. Holmes, *Energy* **2021**, *226*, 120318.

[236] Z. Ji, J. Chen, Z. Guo, Z. Zhao, R. Cai, M. T. P. Rigby, S. J. Haigh, M. Perez-Page, Y. Shen, S. M. Holmes, *J. Energy Chem.* **2022**, *75*, 399.

[237] W. Zhang, Z. Cao, J. Zhang, K. Peng, Q. Ma, Q. Xu, H. Su, *ACS Sustain Chem Eng* **2020**, *8*, 9195.

[238] A. Ignaszak, C. Song, W. Zhu, J. Zhang, A. Bauer, R. Baker, V. Neburchilov, S. Ye, S. Campbell, *Electrochim. Acta* **2012**, *69*, 397.

ADVANCED
SCIENCE NEWS

www.advancedsciencenews.com

ADVANCED
MATERIALS

www.advmat.de

[239] J. Lobato, H. Zamora, J. Plaza, M. A. Rodrigo, *ChemCatChem* **2016**, *8*, 848.

[240] R. Haider, Y. Wen, Z. F. Ma, D. P. Wilkinson, L. Zhang, X. Yuan, S. Song, J. Zhang, *Chem. Soc. Rev.* **2021**, *50*, 1138.

[241] J. Lobato, H. Zamora, J. Plaza, P. Cañizares, M. A. Rodrigo, *Appl. Catal. B* **2016**, *198*, 516.

[242] H. Zhang, H. T. Chung, D. A. Cullen, S. Wagner, U. I. Kramm, K. L. More, P. Zelenay, G. Wu, *Energy Environ. Sci.* **2019**, *12*, 2548.

[243] K. Kumar, L. Dubau, M. Mermoux, J. Li, A. Zitolo, J. Nelayah, F. Jaouen, F. Maillard, *Angew. Chem., Int. Ed.* **2020**, *59*, 3235.

[244] C. C. Lin, F. R. Smith, N. Ichikawa, T. Baba, M. Itow, *Int. J. Chem. Kinet.* **1991**, *23*, 971.

[245] R. Chenitz, U. I. Kramm, M. Lefèvre, V. Glibin, G. Zhang, S. Sun, J. P. Dodelet, *Energy Environ. Sci.* **2018**, *11*, 365.

[246] T. Myles, L. Bonville, R. Maric, *Catalysts* **2017**, *7*, 16.

[247] T. J. Kazdal, S. Lang, F. Kühl, M. J. Hampe, *J. Power Sources* **2014**, *249*, 446.

[248] K. Hooshyari, B. Amini Horri, H. Abdoli, M. Fallah Vostakola, P. Kakavand, P. Salarizadeh, *Energies* **2021**, *14*, 5440.

[249] R. Kerr, H. R. García, M. Rastedt, P. Wagner, S. M. Alfaro, M. T. Romero, C. Terkelsen, T. Steenberg, H. A. Hjuler, *Int. J. Hydrogen Energy* **2015**, *40*, 16860.

[250] Z. Yang, X. Yu, Y. Zhang, G. Xu, *RSC Adv.* **2016**, *6*, 108158.

[251] H. A. Hjuler, K. Azizi, N. Seselj, S. Martinez Alfaro, H. R. Garcia, D. Gromadskyi, L. Hromadska, S. Primdahl, J. O. Jensen, Q. Li, S. Celenk, L. Cleemann, *ECS Trans.* **2021**, *104*, 403.

[252] U. Reimer, B. Schumacher, W. Lehnert, *J. Electrochem. Soc.* **2015**, *162*, F153.

[253] N. Yousfi-Steiner, P. Moçotéguy, D. Candusso, D. Hissel, *J. Power Sources* **2009**, *194*, 130.

[254] K. Yu, D. J. Groom, X. Wang, Z. Yang, M. Gummalla, S. C. Ball, D. Myers, P. J. Ferreira, *Microsc. Microanal.* **2014**, *20*, 482.

[255] J. Zhang, PEM Fuel Cell Electrocatalysts and Catalyst Layers: Fundamentals and Applications, Springer, UK **2008**.

[256] R. L. Borup, J. R. Davey, F. H. Garzon, D. L. Wood, M. A. Inbody, *J. Power Sources* **2006**, *163*, 76.

[257] M. Vega Paredes, A. Garzón Manjón, B. Hill, T. Schwarz, N. A. Rivas, T. Jurzinsky, K. Hengge, F. Mack, C. Scheu, *Nanoscale* **2022**, *14*, 11543.

[258] A. Kannan, Q. Li, L. N. Cleemann, J. O. Jensen, *Fuel Cells* **2018**, *18*, 103.

[259] S. Søndergaard, L. N. Cleemann, J. O. Jensen, N. J. Bjerrum, *Int. J. Hydrogen Energy* **2019**, *44*, 20379.

[260] J. Aragane, H. Urushibata, T. Murahashi, *J. Appl. Electrochem.* **1996**, *26*, 147.

[261] V. Bandlamudi, P. Bujlo, C. Sita, S. Pasupathi, *Mater. Today Proc.* **2018**, *5*, 10602.

[262] T. Søndergaard, L. N. Cleemann, L. Zhong, H. Becker, T. Steenberg, H. A. Hjuler, L. Seerup, Q. Li, J. O. Jensen, *Electrocatalysis* **2018**, *9*, 302.

[263] T. Engl, L. Gubler, T. J. Schmidt, *Energy Technol.* **2016**, *4*, 65.

[264] M. Pawlyta, S. Smykała, B. Liszka, A. Blacha-Grzechnik, M. Krzywiecki, K. Jurkiewicz, A. Jakóbik-Kolon, *Appl. Surf. Sci.* **2022**, *611*, 155637.

[265] J. C. Meier, C. Galeano, I. Katsounaros, J. Witte, H. J. Bongard, A. A. Topalov, C. Baldizzone, S. Mezzavilla, F. Schüth, K. J. J. Mayrhofer, *Beilstein J. Nanotechnol.* **2014**, *5*, 44.

[266] T. J. Schmidt, J. Baurmeister, *J. Power Sources* **2008**, *176*, 428.

[267] S. Yu, L. Xiao, B. C. Benicewicz, *Fuel Cells* **2008**, *8*, 165.

[268] H. L. Nguyen, J. Han, X. L. Nguyen, S. Yu, Y.-M. Goo, D. D. Le, *Energies* **2021**, *14*, 4048.

[269] C. Alegre, A. Lozano, Á. P. Manso, L. Álvarez-Manuel, F. F. Marzo, F. Barreras, *Appl. Energy* **2019**, *250*, 1176.

[270] P. Long, S. Du, Q. Liu, L. Tao, C. Peng, T. Wang, K. Gu, C. Xie, Y. Zhang, R. Chen, S. Lu, Y. Cheng, W. Feng, S. Wang, *Sci. China Mater.* **2022**, *65*, 904.

[271] Y. Devrim, E. D. Arıca, *Int. J. Hydrogen Energy* **2019**, *44*, 18951.

[272] F. Luo, Q. Zhang, Z. Yang, L. Guo, X. Yu, K. Qu, Y. Ling, J. Yang, W. Cai, *ChemCatChem* **2018**, *10*, 5314.

[273] Q. Zhang, Y. Ling, W. Cai, X. Yu, Z. Yang, *Int. J. Hydrogen Energy* **2017**, *42*, 16714.

[274] Z. Yang, T. Fujigaya, N. Nakashima, *J. Mater. Chem. A* **2015**, *3*, 14318.

Nedjeljko Seselj has a background in materials science, electrochemistry, and nanomaterial synthesis. His research has focused on technologies within the energy conversion field, for example, super- and pseudocapacitors, PEM fuel cells, and water electrolysis. He was awarded a Ph.D. degree in chemistry, for a study on graphene-supported, Pt-based nanocatalyst syntheses, applied in low-temperature PEM fuel cells. He currently works as a senior scientist at Blue World Technologies, where his research encompasses: low/high-temperature PEM fuel cells, acid/alkaline water electrolysis, catalyst development, electrode structure studies, and cell testing. He is also a project manager for several energy conversion technology-based external projects, collaborating with international universities and industries.

Silvia Martínez Alfaro has a background in materials science and electrochemistry as a chemical engineer. She wrote her master project on durability and characterization of HT-PEMFCs. Since then, she has taken part in various research studies and European projects on PEM fuel cells and water electrolysis. From 2012 she has worked as Research and development engineer at DPS/Blue World Technologies, where her work focused on HTPEM fuel cell characterization, development of protocols for optimizing test conditions to minimize cell degradation.

Eftychia Bompolaki has a Ph.D. in electrochemistry obtained on non-Pt catalyst layers for PEM fuel electrodes. Her activities focus on research and development for HT-PEM fuel cell technology. Her professional interests lie in R&D catalyst material selection and evaluation, catalyst layer electrode-based optimization, and PEM fuel cell short-term and long-term durability testing.

Lars Nilausen Cleemann is the Team Lead material development at Blue World Technologies. His main focus area is development of materials for HT-PEM systems, to enhance durability and performance. He received his Ph.D. in electrochemistry from the Technical University of Denmark, in 2009 and has been working within the field of HT-PEM fuel cells, since then, first within academia and for the last year at Blue World Technologies.

Tomás Torres is Professor of Organic Chemistry at the Autónoma University of Madrid (UAM) and Associated Senior Scientist at the IMDEA Nanoscience. His research interests include the preparation and properties study of functional nanomaterials. His field of research spans from basic research and applications of porphyrinoids and carbon nanostructures (fullerenes, carbon nanotubes, graphene), in the context of photocatalytic molecular photovoltaics, photocatalytic H_2 production, CO_2 capture/utilization, and photodynamic therapy, with a focus on nanotechnology.

ADVANCED
SCIENCE NEWS

www.advancedsciencenews.com

ADVANCED
MATERIALS

www.advmat.de

Kobra Azizi got a Ph.D. degree in Chemistry (2015) from Tarbiat Modares University, Tehran, Iran, working in catalysis, and completed her formation with a postdoctoral stay (2017–2019) at the Technical University of Denmark (DTU). Since 2020 she has been working as a senior scientist at Danish Power Systems/Blue World Technologies, Denmark. The company is devoted to the development and manufacture of methanol fuel cell components and systems for the automotive and heavy-duty transportation sectors and stationary applications around the world. In addition to various aspects of organic/inorganic synthetic and supramolecular chemistry, her current research interests include the development of new membranes for high-temperature fuel cells.